Article

Influence of Centrifugal Buoyancy in Thermal Convection within a Rotating Spherical Shell

Hidemoto Satake and Toshio Tagawa *

Department of Aeronautics and Astronautics, Tokyo Metropolitan University, Hino 191-0065, Japan
* Correspondence: tagawa-toshio@tmu.ac.jp; Tel.: +81-42-585-8662

Abstract: The dynamo action, which is of importance in the study of the geomagnetism mechanism, is considered to be caused by the convection structure formed inside a rotating spherical shell. This convection structure elongated in the rotation axis is generated by the action of both heat and rotation on the fluid inside a spherical shell. In this study, we analyzed thermal convection in such a rotating spherical shell and attempted to understand the phenomenon of this convective structure. It is known that each value of the Prandtl number, the Ekman number and the Rayleigh number and their balance are important for the generation of such convective structure. We fixed these three parameters and considered the effect of centrifugal buoyancy as the Froude number additionally. To investigate how the effects of centrifugal buoyancy affect the convective structure, we carried out both three-dimensional numerical simulations and linear stability analyses. In particular, we focused on the transition from axisymmetric flow to non-axisymmetric flow having wavenumbers in the toroidal direction and investigated both growth rate and phase velocity of the disturbance. It was found that axisymmetric flow tends to be maintained as the effect of centrifugal buoyancy increases.

Keywords: thermal convection; centrifugal force; numerical simulation; linear stability analysis; spherical shell; buoyancy

1. Introduction

One of the research methods for elucidating the flow of the atmosphere or ocean on the surface of the Earth or the flow of the outer core inside of the Earth is to solve the governing equations numerically. Since the Earth itself rotates around its axis, it is often analyzed based on the equations expressed in the rotating frame of reference. It is a well-known fact that both Coriolis force and centrifugal force appear in the equations of a rotating system, but the centrifugal force based on the rotation speed of the Earth is much smaller than the self-universal gravitational force of the Earth, and therefore, it is usually ignored.

In linear stability analysis, an infinitesimal disturbance is applied to the flow field of the basic state that can be obtained with assuming certain symmetry, and its stability can be determined by examining whether it grows or attenuates with time. The Boussinesq approximation is often used for the analysis of natural convection. In the stability of the Rayleigh–Bénard problem, in which the horizontal fluid layer is heated from below and cooled from above, thermal convection occurs when the heat conduction state is broken. Its critical value is determined only by the Rayleigh number, and it takes various values depending on the thermos-fluid conditions of the upper and lower boundaries.

When such a horizontal fluid layer is placed in a rotating field, centrifugal and Coriolis forces have to be considered in addition to the buoyancy. Chandrasekhar [1] investigated in detail the case where the basic state is motionless and in heat conduction and found that the critical Rayleigh number increases due to the influence of the Coriolis force. However, when the fluid layer has a temperature distribution, since the density also changes with temperature, centrifugal force cannot be a conservative force. In other words, in the

Rayleigh–Bénard problem in a rotating system, the basic state is not in a heat conduction state but may have a weak convection.

This situation can also be applied to thermal convection in a concentric rotating spherical shell. In non-rotating thermal convection, where the inner wall of the concentric spherical shell is heated, the outer wall is cooled, and the self-gravitational force toward the center of the sphere acts; then, the basic state is in complete heat conduction. By using linear stability analysis, it is possible to obtain the critical Rayleigh number depending on the radius ratio and the thermal boundary conditions. On the other hand, in the case of thermal convection in a rotating spherical shell, the basic state may have convection because the combined vector of the self-gravitational force and the centrifugal force does not act toward the center of the sphere.

Although the mechanism of geomagnetism generation is still unclear, it has been considered to be caused by the thermal convection of liquid metal within the outer core region of the Earth. In order to elucidate the Earth dynamo phenomenon, numerical simulations based on MHD (magnetohydrodynamics) equations have been carried out because of the progress of recent computer performance. Particularly, a concentric spherical shell model that is simplified by removing the complexity of the internal structure of the Earth has been targeted.

The research group of Roberts studied the dynamo action generated in the core of the Earth using three-dimensional calculations of a rotating spherical shell [2]. They were also involved in defining the Rayleigh number [3] and reviewed the geodynamo simulations at that time [4]. Such convective flows in rotating spheres were also reviewed and investigated in detail by Busse [5]. Around the same year, Christensen et al. [6] presented a dynamo benchmark solution in collaboration with dynamo researchers around the world. The Boussinesq approximation is often used in the study of thermal convection of a spherical shell related to dynamo action, but there have also been some attempts to consider compressibility of fluid [7–9]. There are also studies focusing on the onset of convection and/or linear stability [10–12]. In recent years, some high-resolution simulations related to thermal convection in the Earth's core were published [13–20]. Miyagoshi et al. [13] performed computer simulation of a magnetohydrodynamic dynamo for rotating thermal convection with an Ekman number of the order of 10^{-7}. Yin et al. [14] performed parallel numerical simulation for thermal convection in the Earth's outer core using a collocated cubed-sphere grid. Šimkanin et al. [15] investigated a thermochemical convection and hydrodynamic dynamos in a spherical shell and considered where inertial effects for a low Prandtl number case prevail. In a recent paper [16], the remarkable developments in numerical geodynamo simulations over the last few years were reviewed. Long et al. [17] investigated the scaling behavior of seven diagnostics over a range of Ekman from 10^{-6} to 10^{-3} using a Prandtl number of unity. Their configuration was used to model Earth's core as defined by the fixed flux thermal boundary conditions, radius ratio 0.35 and a gravity profile that varies linearly with radius.

Quite recently, Silva et al. [18] investigated the relative importance of the helicity and cross-helicity electromotive dynamo effects for self-sustained magnetic field generation by chaotic thermal convection in rotating spherical shells. Simitev and Busse [19] studied the onset of convection in the form of magneto-inertial waves in a rotating fluid sphere permeated by a constant axial electric current. Shebalin [20] developed a model to assess the possible effects of mantle electrical conductivity on the magnetic field values at the core–mantle boundary.

Some dimensionless parameters used in the above simulations (such as the Rayleigh number, the Ekman number, the Prandtl number and the magnetic Prandtl number) that govern the phenomenon are currently set to numerically calculable values instead of using the real Earth's parameters. The Rayleigh number represents the effect of buoyancy, the Ekman number represents the effect of the Coriolis force, the Prandtl number represents the viscosity–heat diffusion ratio, and the magnetic Prandtl number represents the viscosity–magnetic diffusion ratio. The effects of centrifugal force cannot be incorporated even

with these four parameters. Of course, in an isothermal situation, the centrifugal force is a conservative force like gravity, so it is irrelevant to the motion of fluid. However, in non-isothermal cases, the centrifugal force may also invoke buoyancy, similar to the buoyancy caused by the gravitational force.

The effect of centrifugal buoyancy force is recognized to be important in the field of the crystal growth [21]. However, in the field of geodynamo simulation, it has not been sufficiently discussed because it is usually small [8]. In view of this background, a three-dimensional numerical simulation and linear stability analysis were carried out in order to examine the effect of centrifugal buoyancy on thermal convection in a rotating spherical shell, ignoring the dynamo action.

2. Three-Dimensional Numerical Simulation

2.1. Model and Boussinesq Approximation

Figure 1 shows the analysis model considered in this study. A rotating spherical coordinate system was employed to take into account the rotation of the spherical shell. Incompressible Newtonian fluid was assumed, and viscous dissipation was ignored. The physical properties of fluid such as thermal diffusivity and kinematic viscosity except density were assumed to be constant. It was also assumed that the gravitational force acts in the direction toward the center of the sphere, and its magnitude is proportional to the distance from the center. To take the effect of buoyancy into account, the Boussinesq approximation was employed, assuming that the densities for the term of gravitational and centrifugal forces are temperature-dependent. The governing equations in the three-dimensional (3D) simulation were the continuity equation, the equations of motion, and the energy equation in a spherical coordinate system.
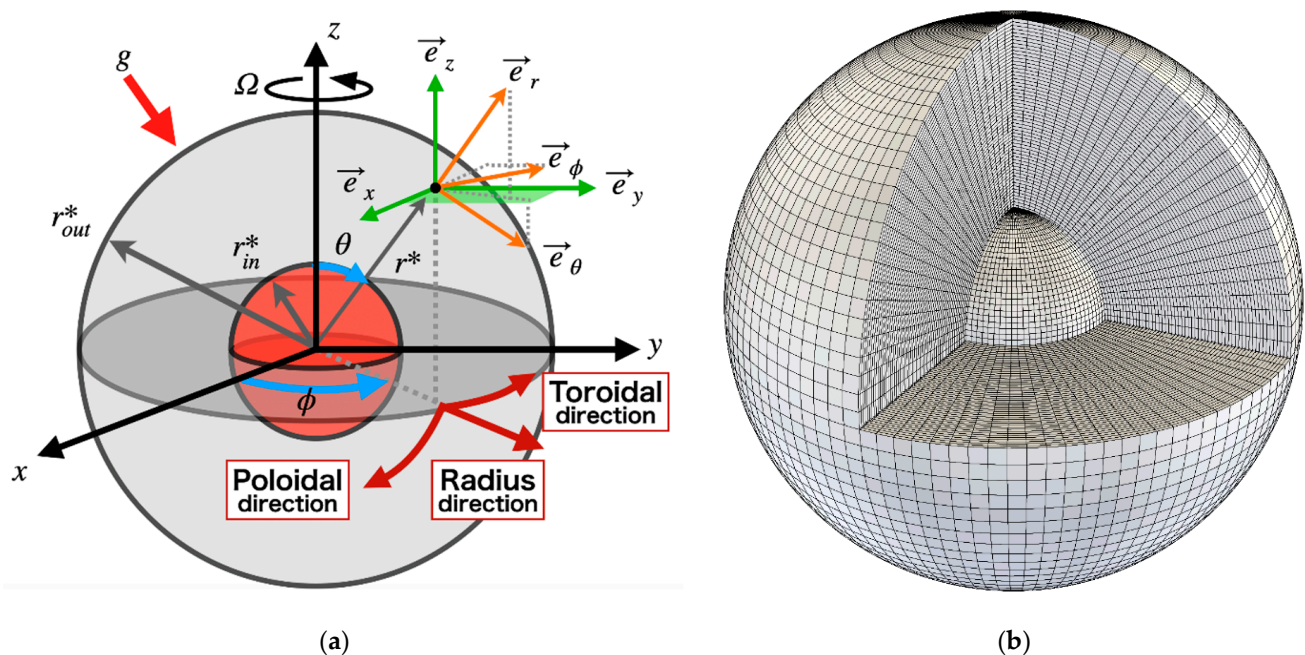

(**a**)   (**b**)

Figure 1. Schematic illustration of the model considered in this work: (**a**) unit vectors and velocity components in the spherical coordinate system; (**b**) an example of computational grids for a spherical shell.

The spherical shell is rotating around the *z*-axis at a constant angular velocity. The angular velocity vector can be expressed using unit vectors as follows:

$$\vec{\Omega} = \Omega \vec{e}_z = \Omega \left[(\cos\theta)\, \vec{e}_r - (\sin\theta)\, \vec{e}_\theta \right] \tag{1}$$

where Ω is the absolute of angular velocity. The relation between the velocities observed from the stationary frame and rotating frame can be given as follows:

$$\vec{u}_S = \vec{u}_R + \vec{\Omega} \times \vec{r} = \vec{u}_R + (r\Omega \sin\theta)\vec{e}_\phi \tag{2}$$

It is noted that the substantial derivative term in the stationary frame of reference can be replaced with the right-hand side of Equation (3), in which the Coriolis force and the centrifugal force appear.

$$\left(\frac{D\vec{u}_S}{Dt}\right)_S = \left(\frac{D\vec{u}_S}{Dt}\right)_R + \vec{\Omega} \times \vec{u}_S = \left(\frac{D\vec{u}_R}{Dt}\right)_R + 2\vec{\Omega} \times \vec{u}_R + \vec{\Omega} \times \left(\vec{\Omega} \times \vec{r}\right) \tag{3}$$

The subscripts S and R represent the quantity observed from the stationary and rotating frame, respectively. From the rotating frame of reference, the centrifugal force and the Coriolis force can be expressed using the spherical coordinate as follows:

$$2\vec{\Omega} \times \vec{u}_R = \left[(-2\Omega u_\phi \sin\theta)\vec{e}_r + (-2\Omega u_\phi \cos\theta)\vec{e}_\theta + (2\Omega u_\theta \cos\theta + 2\Omega u_r \sin\theta)\vec{e}_\phi\right]_R \tag{4}$$

$$\vec{\Omega} \times \left(\vec{\Omega} \times \vec{r}\right) = \left(-\Omega^2 r \sin^2\theta\right)\vec{e}_r + \left(-\Omega^2 r \sin\theta\cos\theta\right)\vec{e}_\theta. \tag{5}$$

The momentum equations in the rotating frame of reference can be expressed using the three unit vectors of the spherical coordinate system, where, the gravitational acceleration acts towards the center of sphere, and its strength is proportional to the radius. The subscript R which represents the quantity observed from the rotating frame is omitted hereafter.

$$\rho\frac{D\vec{u}}{Dt} = -\nabla p + \mu\nabla^2\vec{u} + \left(-\rho\frac{g_0}{r_{out}}r + \rho\Omega^2 r \sin^2\theta + 2\rho\Omega u_\phi \sin\theta\right)\vec{e}_r$$
$$+\left(\rho\Omega^2 r \sin\theta\cos\theta + 2\rho\Omega u_\phi \cos\theta\right)\vec{e}_\theta - 2\rho\Omega(u_r \sin\theta + u_\theta \cos\theta)\vec{e}_\phi \tag{6}$$

When the fluid temperature within the spherical shell is uniform, the buoyant convection does not take place when it is observed from the rotating frame of reference. Hence, the above momentum equations simply indicate force balance between the pressure gradient and the conservative forces as shown in Equation (7).

$$\frac{\partial p_s}{\partial r} = \rho_0\Omega^2 r \sin^2\theta - \rho_0\frac{g_0}{r_{out}}r, \quad \frac{1}{r}\frac{\partial p_s}{\partial\theta} = \rho_0\Omega^2 r \sin\theta\cos\theta, \quad \frac{1}{r\sin\theta}\frac{\partial p_s}{\partial\phi} = 0 \tag{7}$$

where p_s is the static pressure when the convection does not take place, and ρ_0 is the constant fluid density at a reference temperature T_0. By using Equation (7), the static pressure distribution can be easily obtained as follows:

$$p_s(r,\theta) = \frac{1}{2}\rho_0 r^2\left(\Omega^2 \sin^2\theta - \frac{g_0}{r_{out}}\right) + \text{Const.} \tag{8}$$

Then, by subtracting Equation (7) from the momentum equations, the density difference is approximated with the temperature difference by using the Taylor expansion together with the thermal expansion coefficient as follows:

$$\rho - \rho_0 \cong \left(\frac{\partial\rho}{\partial T}\right)_0 (T - T_0) = -\rho_0\beta_0(T - T_0). \tag{9}$$

Finally, the momentum equations with the Boussinesq approximation are expressed in Equation (10).

$$\frac{D\vec{u}}{Dt} = -\frac{1}{\rho_0}\nabla(p - p_s) + \frac{\mu}{\rho_0}\nabla^2\vec{u} + \left[\beta_0\left(T - T_0\right)r\left(\frac{g_0}{r_{out}} - \Omega^2\sin^2\theta\right) + 2\Omega u_\phi\sin\theta\right]\vec{e}_r$$
$$+\left[-\beta_0\left(T - T_0\right)\Omega^2 r\sin\theta\cos\theta + 2\Omega u_\phi\cos\theta\right]\vec{e}_\theta + \left[-2\Omega(u_r\sin\theta + u_\theta\cos\theta)\right]\vec{e}_\phi \tag{10}$$

2.2. Dimensionless Governing Equations

Dimensionless governing equations expressed in the spherical coordinate system are summarized as follows [22–24]:

Conservation law of mass:

$$\frac{1}{r^{*2}}\frac{\partial\left(r^{*2}u_r^*\right)}{\partial r^*} + \frac{1}{r^*\sin\theta}\frac{\partial\left(u_\theta^*\sin\theta\right)}{\partial\theta} + \frac{1}{r^*\sin\theta}\frac{\partial u_\phi^*}{\partial\phi} = 0 \tag{11}$$

Momentum equation—radius direction:

$$\frac{\partial u_r^*}{\partial t^*} + u_r^*\frac{\partial u_r^*}{\partial r^*} + \frac{u_\theta^*}{r^*}\frac{\partial u_r^*}{\partial\theta} + \frac{u_\phi^*}{r^*\sin\theta}\frac{\partial u_r^*}{\partial\phi} - \frac{u_\theta^{*2} + u_\phi^{*2}}{r^*}$$
$$= -\frac{\partial p^*}{\partial r^*} + RaPrT^*r^*\left(\frac{1}{r_{out}^*} - Fr^2\sin^2\theta\right) + \frac{Pr}{Ek}u_\phi^*\sin\theta + Pr\left(\nabla^{*2}u_r^* - \frac{2u_r^*}{r^{*2}} - \frac{2}{r^{*2}}\frac{\partial u_\theta^*}{\partial\theta} - \frac{2u_\theta^*\cot\theta}{r^{*2}} - \frac{2}{r^{*2}\sin\theta}\frac{\partial u_\phi^*}{\partial\phi}\right) \tag{12}$$

Momentum equation—poloidal direction:

$$\frac{\partial u_\theta^*}{\partial t^*} + u_r^*\frac{\partial u_\theta^*}{\partial r^*} + \frac{u_\theta^*}{r^*}\frac{\partial u_\theta^*}{\partial\theta} + \frac{u_\phi^*}{r^*\sin\theta}\frac{\partial u_\theta^*}{\partial\phi} + \frac{u_r^*u_\theta^* - u_\phi^{*2}\cot\theta}{r^*}$$
$$= -\frac{1}{r^*}\frac{\partial p^*}{\partial\theta} - RaPrFr^2T^*r^*\sin\theta\cos\theta + \frac{Pr}{Ek}u_\phi^*\cos\theta + Pr\left(\nabla^{*2}u_\theta^* + \frac{2}{r^{*2}}\frac{\partial u_r^*}{\partial\theta} - \frac{u_\theta^*}{r^{*2}\sin^2\theta} - \frac{2\cos\theta}{r^{*2}\sin^2\theta}\frac{\partial u_\phi^*}{\partial\phi}\right) \tag{13}$$

Momentum equation—toroidal direction:

$$\frac{\partial u_\phi^*}{\partial t^*} + u_r^*\frac{\partial u_\phi^*}{\partial r^*} + \frac{u_\theta^*}{r^*}\frac{\partial u_\phi^*}{\partial\theta} + \frac{u_\phi^*}{r^*\sin\theta}\frac{\partial u_\phi^*}{\partial\phi} + \frac{u_r^*u_\phi^*}{r^*} + \frac{u_\phi^*u_\theta^*\cot\theta}{r^*}$$
$$= -\frac{1}{r^*\sin\theta}\frac{\partial p^*}{\partial\phi} - \frac{Pr}{Ek}(u_r^*\sin\theta + u_\theta^*\cos\theta) + Pr\left(\nabla^{*2}u_\phi^* - \frac{u_\phi^*}{r^{*2}\sin^2\theta} + \frac{2}{r^{*2}\sin\theta}\frac{\partial u_r^*}{\partial\phi} + \frac{2\cos\theta}{r^{*2}\sin^2\theta}\frac{\partial u_\theta^*}{\partial\phi}\right) \tag{14}$$

Energy equation:

$$\frac{\partial T^*}{\partial t^*} + u_r^*\frac{\partial T^*}{\partial r^*} + \frac{u_\theta^*}{r^*}\frac{\partial T^*}{\partial\theta} + \frac{u_\phi^*}{r^*\sin\theta}\frac{\partial T^*}{\partial\phi} = \nabla^{*2}T^* \tag{15}$$

where the dimensionless operator ∇^{*2} is defined as follows:

$$\nabla^{*2} = \frac{1}{r^{*2}}\frac{\partial}{\partial r^*}\left(r^{*2}\frac{\partial}{\partial r^*}\right) + \frac{1}{r^{*2}\sin\theta}\frac{\partial}{\partial\theta}\left(\sin\theta\frac{\partial}{\partial\theta}\right) + \frac{1}{r^{*2}\sin^2\theta}\frac{\partial^2}{\partial\phi^2} \tag{16}$$

The dimensionless variables and non-dimensional numbers are defined as follows:

$$r^* = \frac{r}{r_0} \quad, \quad u_r^* = \frac{u_r}{u_0} \quad, \quad u_\theta^* = \frac{u_\theta}{u_0} \quad, \quad u_\phi^* = \frac{u_\phi}{u_0} \quad, \quad T^* = \frac{T - T_0}{T_h - T_c} \quad, \quad t^* = \frac{t}{t_0} \quad, \quad p^* = \frac{p - p_s}{p_0}$$
$$Ra = \frac{\beta_0(T_h - T_c)r_0^3 g_0}{\nu\alpha} \quad, \quad Pr = \frac{\nu}{\alpha} \quad, \quad Ek = \frac{\nu}{2\Omega r_0^2} \quad, \quad Fr = \sqrt{\frac{\Omega^2 r_0}{g_0}} \quad, \quad \eta = \frac{r_{in}}{r_{out}} \tag{17}$$

Ra indicates the Rayleigh number, *Pr* is the Prandtl number, *Ek* is the Ekman number, and η is the radius ratio. The Rayleigh number represents the effect of buoyancy, the Ekman number represents the effect of the Coriolis force, and the Prandtl number represents the viscosity–heat diffusion ratio, where reference values are defined as follows:

$$r_0 = r_{out} - r_{in} \quad, \quad u_0 = \frac{\alpha}{r_0} \quad, \quad p_0 = \frac{\rho_0\alpha^2}{r_0^2} \quad, \quad t_0 = \frac{r_0^2}{\alpha} \quad, \quad T_0 = \frac{T_h + T_c}{2} \tag{18}$$

The characteristic length is the gap between the outer wall and the inner wall. The characteristic velocity is defined using the thermal diffusity of fluid. The reference temperature is taken at the average temperature between the hot wall and the cold wall. The above

non-dimensional equations can be solved in several ways. For example, Ozoe et al. [22] eliminated the pressure terms from the governing equations and solved the three-dimensional vorticity transport equations. However, its derivation is quite complicated, and therefore, we solved the above governing equations by including the pressure terms using a finite difference method.

2.3. Computational Conditions

2.3.1. Initial Conditions

The initial conditions for velocity field are stationary, while those for temperature field are slightly disturbed using a random number generation as shown in Equation (19), where *mt* represents a random number generated [25] by the Mersenne Twister.

$$T_{init}^* = 1 + r_{out}^* - r^* + \frac{mt}{1000.0} \quad, \quad u_{r\,init}^* = u_{\theta\,init}^* = u_{\phi\,init}^* = 0, \quad p_{init}^* = 0 \qquad (19)$$

2.3.2. Boundary Conditions

Isothermal heating is assumed at the inner boundary, while isothermal cooling is adopted at the outer boundary. The velocity is no-slip/no-penetration at the two boundaries. Regarding the pressure, the radial gradient is set to zero. The Ozoe and Toh method [26,27] was applied to treat the singularities at the North and South Poles.

$$T^* = 1 \quad, \quad u_r^* = u_\theta^* = u_\phi^* = 0 \quad, \quad \frac{\partial p^*}{\partial r^*} = 0 \qquad at \quad r^* = r_{in}^* = \frac{\eta}{1 - \eta} \qquad (20)$$

$$T^* = 0 \quad, \quad u_r^* = u_\theta^* = u_\phi^* = 0 \quad, \quad \frac{\partial p^*}{\partial r^*} = 0 \qquad at \quad r^* = r_{out}^* = \frac{1}{1 - \eta} \qquad (21)$$

2.3.3. Computational Parameters and Numerical Strategy

In this study, the radius ratio, the Rayleigh number, the Prandtl number and the Ekman number were fixed, while the Froude number, which represents the effect of the centrifugal buoyancy force, was varied for six cases as shown in Table 1. These dimensionless parameters are far from those of the Earth dynamo. The Rayleigh numbers are much larger, and the Ekman numbers are much smaller, so such computation cannot be realized even by using modern supercomputers. Therefore, considering the cases of previous research, the combination shown in Table 1 was employed as dimensionless parameters.

Table 1. Parameters of the present analysis.

Radius Ratio	Rayleigh Number	Prandtl Number	Ekman Number	Froude Number
η	Ra	Pr	Ek	Fr
0.35	4.5×10^4	1.0	1.0×10^{-3}	0.0 0.1 0.2 0.3 0.4 0.5

The analyses were conducted by a GPU (Graphics Processing Unit) parallel computation using the programming language of C++AMP (C++ Accelerated Massive Parallelism). The computational method was based on the finite difference method together with the Red and Black HSMAC (Highly Simplified Maker and Cell) method. The computational domain was discretized on a staggered grid system. As for the discretization method, the four-step Runge–Kutta method was introduced for the time-derivative term, and the second-order central difference method was applied for the others, such as convective,

pressure, and diffusion terms. As a pressure correction judgment condition, an iterative correction procedure was performed until the maximum value of velocity divergence became 10^{-3} or less.

2.4. Results

2.4.1. Validation of the Present Code Developed

In order to verify the validity of the code developed for the thermal convection analysis in a spherical shell using the finite difference method, we compared kinetic energy between the present result and that of the dynamo benchmark solution [6]. The value of kinetic energy was taken at a quasi-steady state. The definition of the kinetic energy is shown in Equation (22). In order to verify the grid-size dependence, the initial temperature conditions in the dynamo benchmark paper shown in Equation (23) were adopted.

$$E_{kin} = \frac{1}{2V} \int_V \left| \vec{u}^* \right|^2 dV \tag{22}$$

$$T_{init}^* = \frac{r_{out}^* r_{in}^*}{r^*} - r_{in}^* + \frac{210A}{\sqrt{17920\pi}} \left(1 - 3x^2 + 3x^4 - x^6 \right) \sin^4 \theta \cos 4\phi \tag{23}$$

where $A = 0.1$, $x = 2r^* - r_{in}^* - r_{out}^*$. The computational conditions for the benchmark problem are summarized in Table 2.

Table 2. Parameters of the benchmark problem.

Radius Ratio	Rayleigh Number	Prandtl Number	Ekman Number	Froude Number
η	Ra	Pr	Ek	Fr
0.35	1.0×10^5	1.0	5.0×10^{-4}	0.0

The number of grids was changed in five ways for verification, as shown in Table 3. For grid dependence, in addition to the value of kinetic energy at the quasi-steady state, the visualizations of toroidal velocity distribution in the equatorial cross section are compared, as shown in Figure 2. There are not significant differences among the five figures.

Table 3. Tests of grid dependency.

-	Number of Grids ($N_r \times N_\theta \times N_\phi$)	Time Increment Δt^*
Test 1	$30 \times 30 \times 72$	3.0×10^{-6}
Test 2	$40 \times 40 \times 80$	1.0×10^{-6}
Test 3	$50 \times 50 \times 100$	6.0×10^{-7}
Test 4	$56 \times 56 \times 112$	5.0×10^{-7}
Test 5	$64 \times 64 \times 128$	3.0×10^{-7}

Figure 3 shows the comparison between the present five tests and the benchmark solution for the kinetic energy. It can be understood that the temporal history of the kinetic energy inside the spherical shell at each grid number has a qualitatively similar solution. Table 4 shows a summary of the grid-size dependence on the converged values of the kinetic energy. The lower values in Table 4 indicate the relative error from the benchmark value. From this result, it can be confirmed that the value obtained by the present analysis approaches the benchmark solution as the number of grids is increased. Table 4 also shows that the relative error is about 2.6% when the number of grids more than $56 \times 56 \times 112$ was employed. It was judged that there is no problem with the quantitative validity of the present analysis code. In this study, the number of grids $56 \times 56 \times 112$ was employed because we considered that it is sufficient for this system.
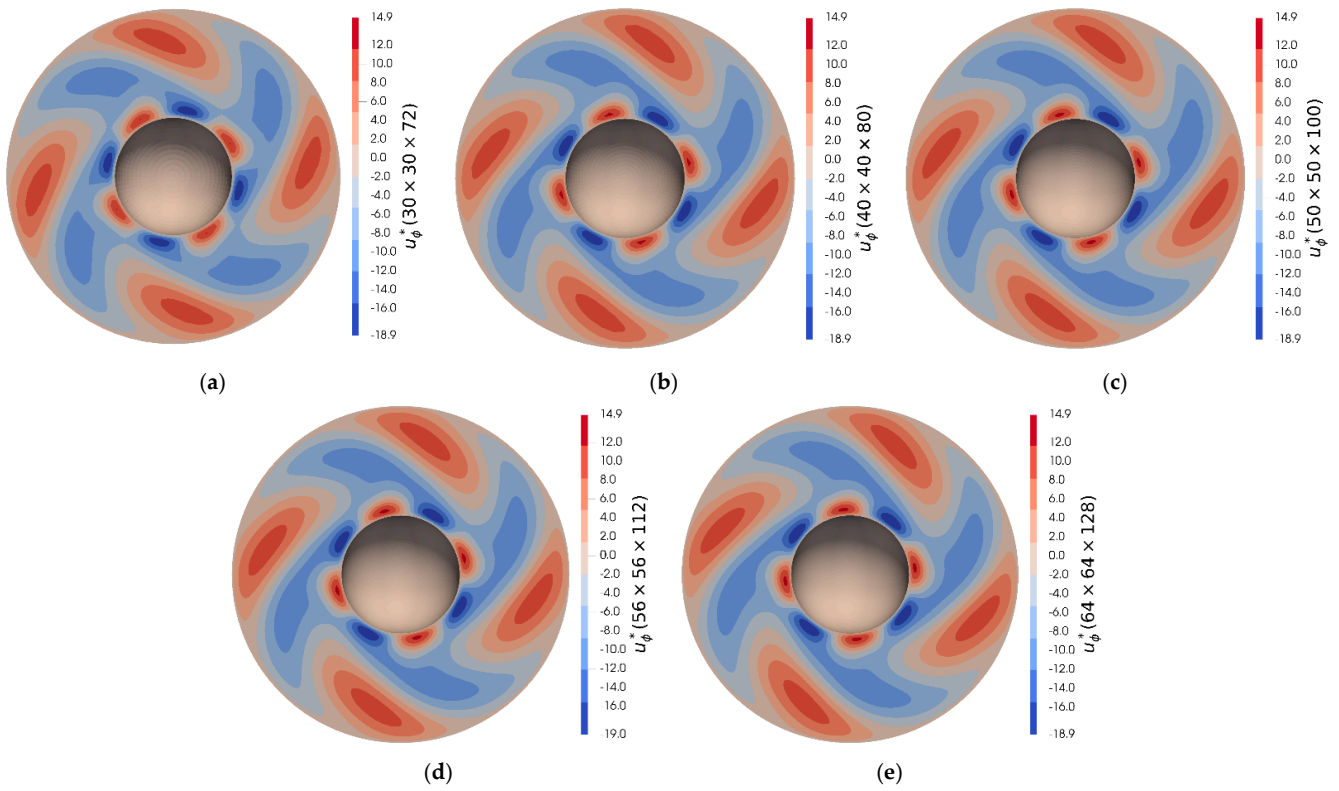
Figure 2. Dependency of grid size on the toroidal component of velocity at the equatorial cross section at $t^* = 1.0$: (**a**) test 1; (**b**) test 2; (**c**) test 3; (**d**) test 4; (**e**) test 5.
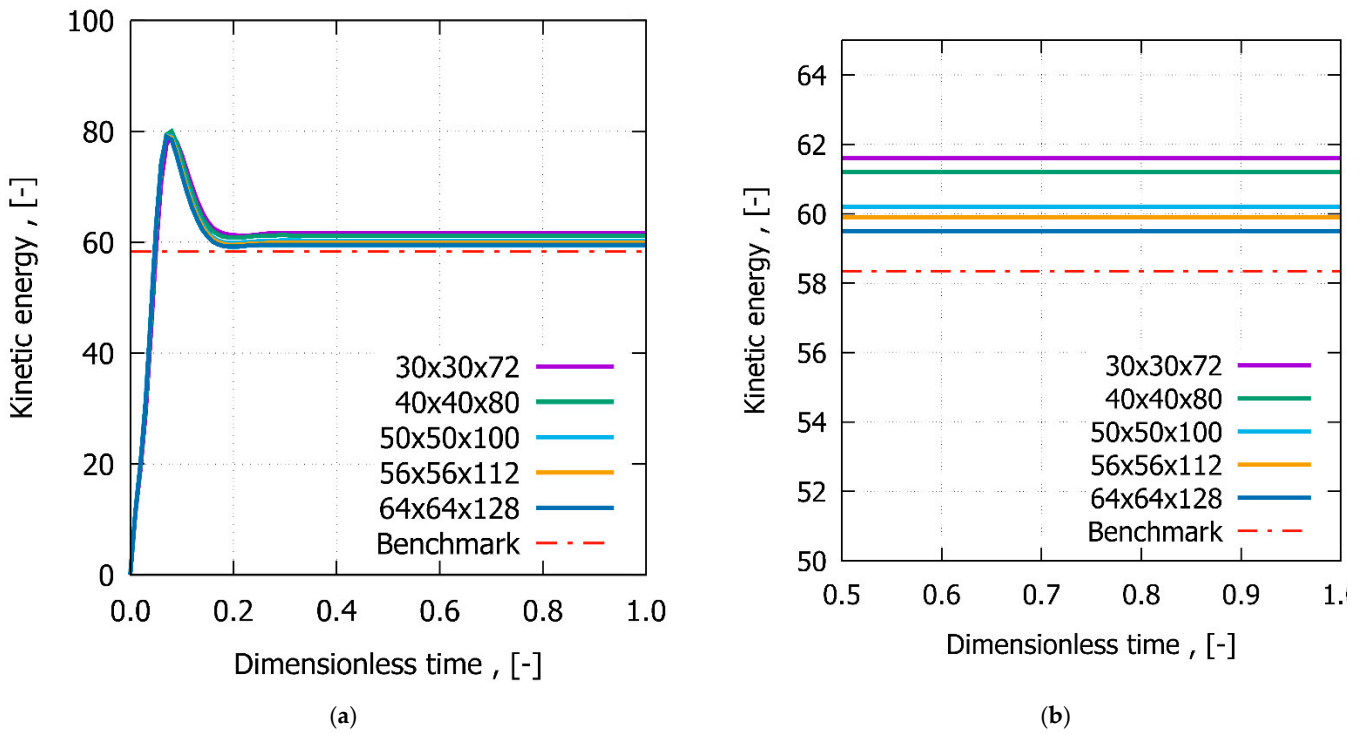

Figure 3. (**a**) Evolution of the kinetic energy for the five tests and comparison with the benchmark value; (**b**) the enlarged one for the quasi-state.

Table 4. Dependences of grid size on the kinetic energy and relative error.

$N_r \times N_\theta \times N_\phi$	$30 \times 30 \times 72$	$40 \times 40 \times 80$	$50 \times 50 \times 100$	$56 \times 56 \times 112$	$64 \times 64 \times 128$	Benchmark
E_{kin}	61.62	61.24	60.25	59.88	59.53	58.35
$\frac{E_{kin}-58.35}{58.35} \times 100$	5.60	4.95	3.25	2.62	2.03	-

We mention the dependence of the velocity divergence on numerical results. In this study, iterative correction was performed so that the maximum value of the velocity divergence was less than 10^{-3}. We checked whether there was any change when the set value was 10^{-6} for the $56 \times 56 \times 112$ grid-size case. As a result, the kinetic energy was 59.8776 irrespective of the set value 10^{-3} or 10^{-6}. Since the same result was obtained, it can be concluded that the setting condition of the velocity divergence value at 10^{-3} is even sufficient.

2.4.2. Effect of the Froude Number

As shown in Table 1, we considered how the convection structure inside the spherical shell changes when the Froude number, that is, the effect of centrifugal buoyancy, is changed. From Figure 4, it can be recognized that the timing of kinetic energy amplification is delayed as the Froude number becomes larger. In addition, it can be seen that as the effect of centrifugal buoyancy increases, a rather flat region exists until just before the begging of amplification. This can be explained from the viewpoint of flow instability, so we will reconsider it based on the results after performing linear stability analyses in Section 5.1.
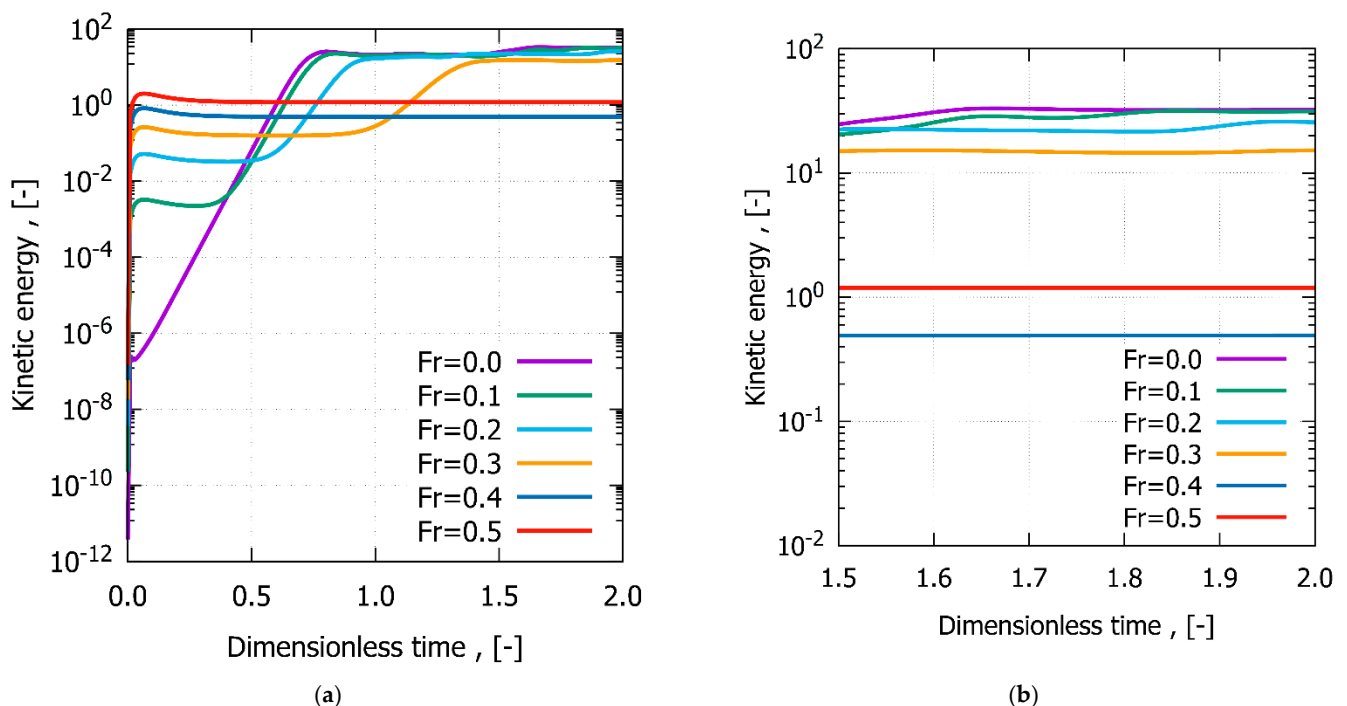

(**a**)   (**b**)

Figure 4. (**a**) Temporal evolution of the kinetic energy using logarithmic scale for the several values of the Froude number; (**b**) the enlarged one for the dimensionless time from 1.5 to 2.0.

Figure 5 shows the equatorial cross-sectional distribution of the toroidal velocity at the dimensionless time 2.0. It can be seen that four wavenumbers are generated at $Fr = 0.0$ in which no effect of centrifugal buoyancy is considered. At $Fr = 0.1$ and $Fr = 0.2$, however, the wavenumber is reduced to three, and it can be seen that the effect of centrifugal buoyancy appears on the wavenumber. At $Fr = 0.3$, the flow field is like the transition between three and four wavenumbers, and the structure is such that the wavenumbers cannot be uniquely determined. At $Fr = 0.4$ and $Fr = 0.5$, the flow field is almost axisymmetric at the

dimensionless time 2.0, and since the wavenumber does not appear, it can be recognized that the state at these Froude numbers is considered to be near the critical value or below the critical value.
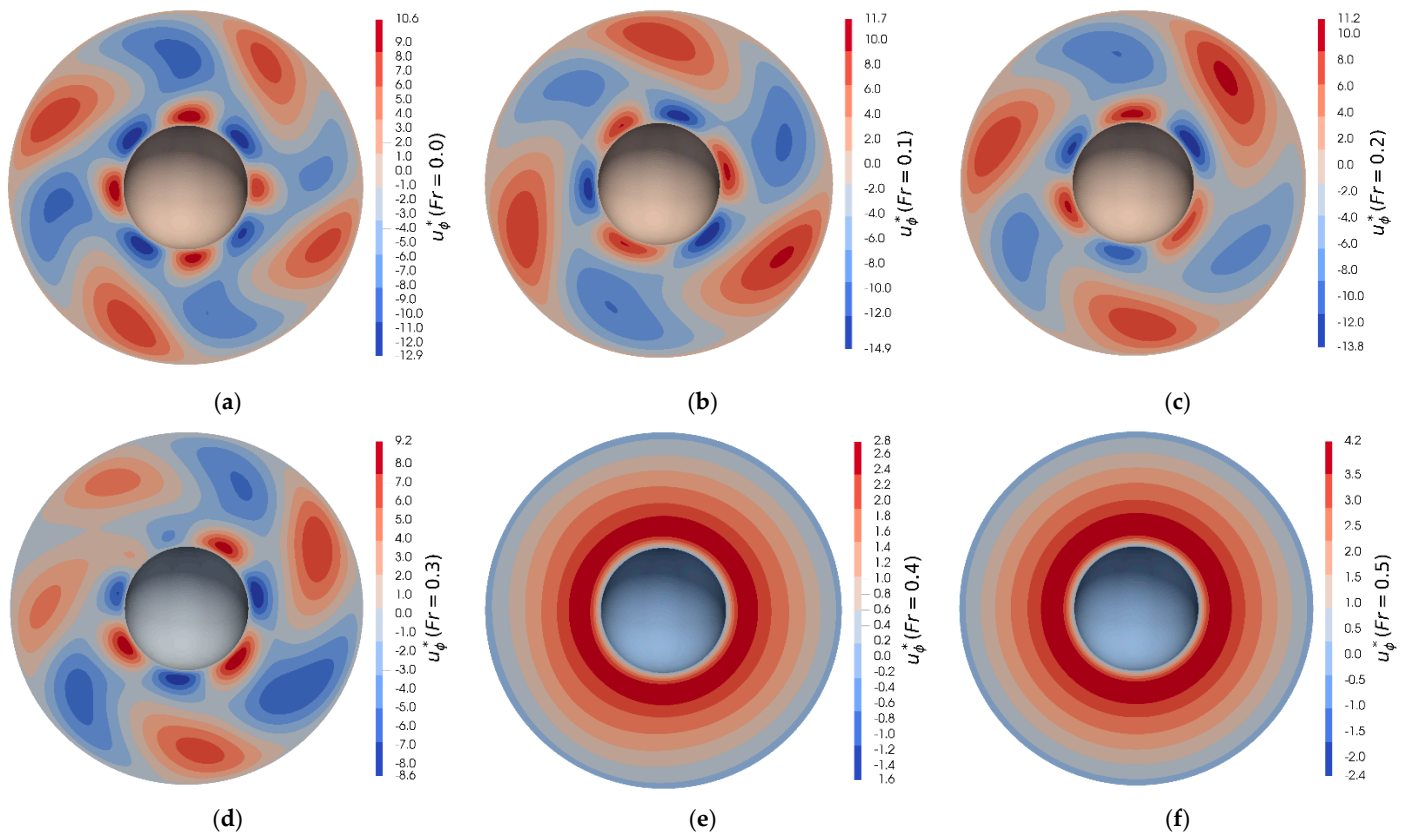

Figure 5. Effect of the Froude number on the toroidal component of velocity at the equatorial cross section at $t^* = 2.0$: (**a**) $Fr = 0$; (**b**) $Fr = 0.1$; (**c**) $Fr = 0.2$; (**d**) $Fr = 0.3$; (**e**) $Fr = 0.4$; (**f**) $Fr = 0.5$.

3. Linear Stability Analysis (LSA)

In this section, a linear stability analysis is performed in order to approach from a viewpoint of flow stability theory. In the linear stability analysis, a steady basic state in which the influence of disturbance is removed from the flow field is firstly obtained, and then its stability is analyzed. In the present problem, convection is caused by the influence of azimuthally periodic disturbance, so the basic state is obtained by introducing the axisymmetric assumption. Furthermore, by superposing the disturbance into the basic state, the stability of the basic flow field can be discussed.

3.1. Model for LSA

The model in the linear stability analysis is shown in Figure 6. Only the half hemisphere of the spherical annulus is analyzed for obtaining both the basic state and its linear stability.
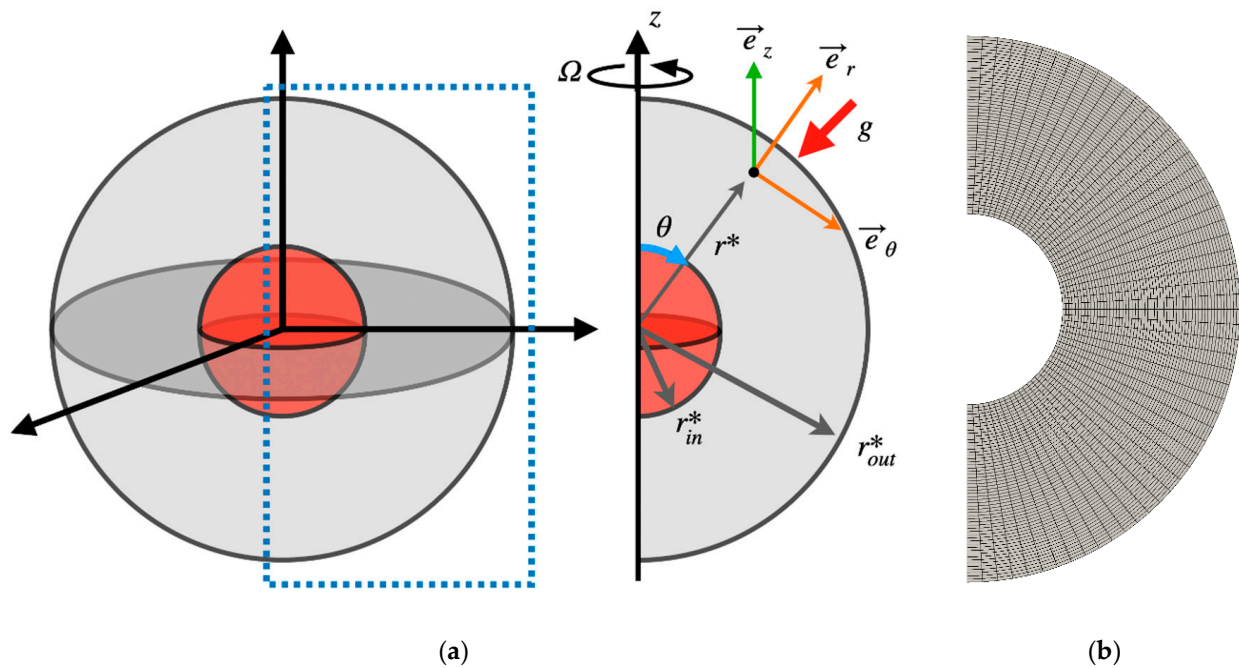
Figure 6. Model considered for the linear stability analysis: (**a**) spherical annulus; (**b**) computational grid system.

3.2. Basic State

As a method for obtaining the basic state, the computation assuming axial symmetry is carried out as the first stage, and the obtained numerical solution that does not change with time is used as the basic state for the linear stability analysis. The analyses were conducted by a GPU parallel computation with using the programming language of C++AMP. The analysis method is based on the finite difference method with the Red and Black HSMAC method as explained in Section 2. The discretization method is the Euler explicit method for the time-derivative term, and the second-order central difference method is applied for the convective, pressure, and diffusion terms. As a pressure correction judgement condition, the same criterion was used as mentioned in Section 2.3.3.

3.2.1. Dimensionless Governing Equations for the Basic State

Conservation law of mass:

$$\frac{1}{r^{*2}}\frac{\partial\left(r^{*2}\overline{u}_r^*\right)}{\partial r^*} + \frac{1}{r^*\sin\theta}\frac{\partial\left(\overline{u}_\theta^*\sin\theta\right)}{\partial\theta} = 0 \tag{24}$$

Momentum equation—radius direction:

$$\overline{u}_r^*\frac{\partial\overline{u}_r^*}{\partial r^*} + \frac{\overline{u}_\theta^*}{r^*}\frac{\partial\overline{u}_r^*}{\partial\theta} - \frac{\overline{u}_\theta^{*2}+\overline{u}_\phi^{*2}}{r^*}$$
$$= -\frac{\partial\overline{p}^*}{\partial r^*} + RaPr\overline{T}^*r^*\left(\frac{1}{r_{out}^*} - Fr^2\sin^2\theta\right) + \frac{Pr}{Ek}\overline{u}_\phi^*\sin\theta + Pr\left(\overline{\nabla}^{*2}\overline{u}_r^* - \frac{2\overline{u}_r^*}{r^{*2}} - \frac{2}{r^{*2}}\frac{\partial\overline{u}_\theta^*}{\partial\theta} - \frac{2\overline{u}_\theta^*\cot\theta}{r^{*2}}\right) \tag{25}$$

Momentum equation—poloidal direction:

$$\overline{u}_r^*\frac{\partial\overline{u}_\theta^*}{\partial r^*} + \frac{\overline{u}_\theta^*}{r^*}\frac{\partial\overline{u}_\theta^*}{\partial\theta} + \frac{\overline{u}_r^*\overline{u}_\theta^* - \overline{u}_\phi^{*2}\cot\theta}{r^*}$$
$$= -\frac{1}{r^*}\frac{\partial\overline{p}^*}{\partial\theta} - RaPrFr^2\overline{T}^*r^*\sin\theta\cos\theta + \frac{Pr}{Ek}\overline{u}_\phi^*\cos\theta + Pr\left(\overline{\nabla}^{*2}\overline{u}_\theta^* + \frac{2}{r^{*2}}\frac{\partial\overline{u}_r^*}{\partial\theta} - \frac{\overline{u}_\theta^*}{r^{*2}\sin^2\theta}\right) \tag{26}$$

Momentum equation—toroidal direction:

$$\overline{u}_r^*\frac{\partial\overline{u}_\phi^*}{\partial r^*} + \frac{\overline{u}_\theta^*}{r^*}\frac{\partial\overline{u}_\phi^*}{\partial\theta} + \frac{\overline{u}_r^*\overline{u}_\phi^*}{r^*} + \frac{\overline{u}_\phi^*\overline{u}_\theta^*\cot\theta}{r^*} = -\frac{Pr}{Ek}\left(\overline{u}_r^*\sin\theta + \overline{u}_\theta^*\cos\theta\right) + Pr\left(\overline{\nabla}^{*2}\overline{u}_\phi^* - \frac{\overline{u}_\phi^*}{r^{*2}\sin^2\theta}\right) \tag{27}$$

Energy equation:

$$\overline{u}_r^* \frac{\partial \overline{T}^*}{\partial r^*} + \frac{\overline{u}_\theta^*}{r^*} \frac{\partial \overline{T}^*}{\partial \theta} = \overline{\nabla}^{*2} \overline{T}^* \tag{28}$$

where $\overline{\nabla}^{*2}$ is defined as follows:

$$\overline{\nabla}^{*2} = \frac{1}{r^{*2}} \frac{\partial}{\partial r^*} \left(r^{*2} \frac{\partial}{\partial r^*} \right) + \frac{1}{r^{*2} \sin \theta} \frac{\partial}{\partial \theta} \left(\sin \theta \frac{\partial}{\partial \theta} \right) \tag{29}$$

Dimensionless variables and non-dimensional numbers are as follows:

$$
\begin{aligned}
r^* = \frac{r}{r_0} \quad, \quad \overline{u}_r^* = \frac{\overline{u}_r}{u_0} \quad, \quad \overline{u}_\theta^* = \frac{\overline{u}_\theta}{u_0} \quad, \quad \overline{u}_\phi^* = \frac{\overline{u}_\phi}{u_0} \quad, \quad \overline{T}^* = \frac{\overline{T} - T_0}{T_h - T_c} \quad, \quad \overline{p}^* = \frac{\overline{p} - p_s}{p_0} \\
Ra = \frac{\beta_0 (T_h - T_c) r_0^3 g_0}{\nu \alpha} \quad, \quad Pr = \frac{\nu}{\alpha} \quad, \quad Ek = \frac{\nu}{2\Omega r_0^2} \quad, \quad Fr = \sqrt{\frac{\Omega^2 r_0}{g_0}}
\end{aligned}
\tag{30}
$$

Reference values are defined as follows:

$$t_0 = \frac{r_0^2}{\alpha} \quad, \quad r_0 = r_{out} - r_{in} \quad, \quad u_0 = \frac{\alpha}{r_0} \quad, \quad p_0 = \frac{\rho_0 \alpha^2}{r_0^2} \quad, \quad T_0 = \frac{T_h + T_c}{2} \tag{31}$$

3.2.2. Initial Conditions

The initial conditions are set as follows:

$$T_{init}^* = u_{r\,init}^* = u_{\theta\,init}^* = u_{\phi\,init}^* = p_{init}^* = 0 \tag{32}$$

3.2.3. Boundary conditions

The boundary conditions at the inner and outer walls are set as follows:

$$T^* = 1 \quad, \quad u_r^* = u_\theta^* = u_\phi^* = 0 \quad, \quad \frac{\partial p^*}{\partial r^*} = 0 \qquad at \quad r^* = r_{in}^* \tag{33}$$

$$T^* = 0 \quad, \quad u_r^* = u_\theta^* = u_\phi^* = 0 \quad, \quad \frac{\partial p^*}{\partial r^*} = 0 \qquad at \quad r^* = r_{out}^* \tag{34}$$

whereas those at the axis of rotation are as follows:

$$\frac{\partial T^*}{\partial \theta} = \frac{\partial u_r^*}{\partial \theta} = u_\theta^* = u_\phi^* = \frac{\partial p^*}{\partial \theta} = 0 \qquad at \quad \theta = 0, \pi \tag{35}$$

3.2.4. Results

In order to obtain the basic state, the analysis was carried out with a grid number of 56×56, a dimensionless terminal time of 1.5, and a time increment of 1.0×10^{-5}. Figure 7 shows the temporal evolution of toroidal velocity. It is recognized that the analysis for each Froude number was calculated successfully up to the steady state. Figure 8 shows the contour maps of velocity magnitude in a meridional cross section at the steady state of $t^* = 1.5$. In the flow field of $Fr = 0$, the velocity is negligibly small, whereas in $Fr = 0.1$ or more, a high velocity region is generated near the inner boundary. As a whole tendency for $Fr = 0.1$ or more, it can be recognized that the steady value of the toroidal velocity tends to increase as the effect of centrifugal buoyancy increases.
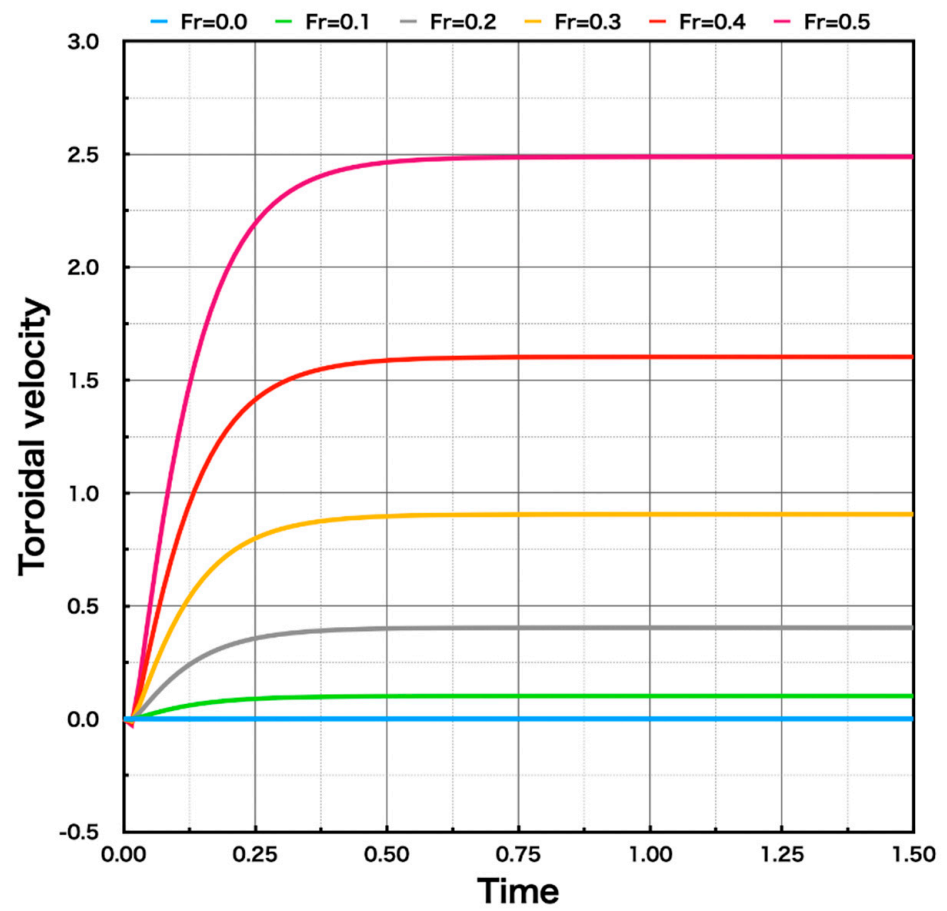
Figure 7. Temporal evolution of the toroidal velocity for different values of the Froude number.
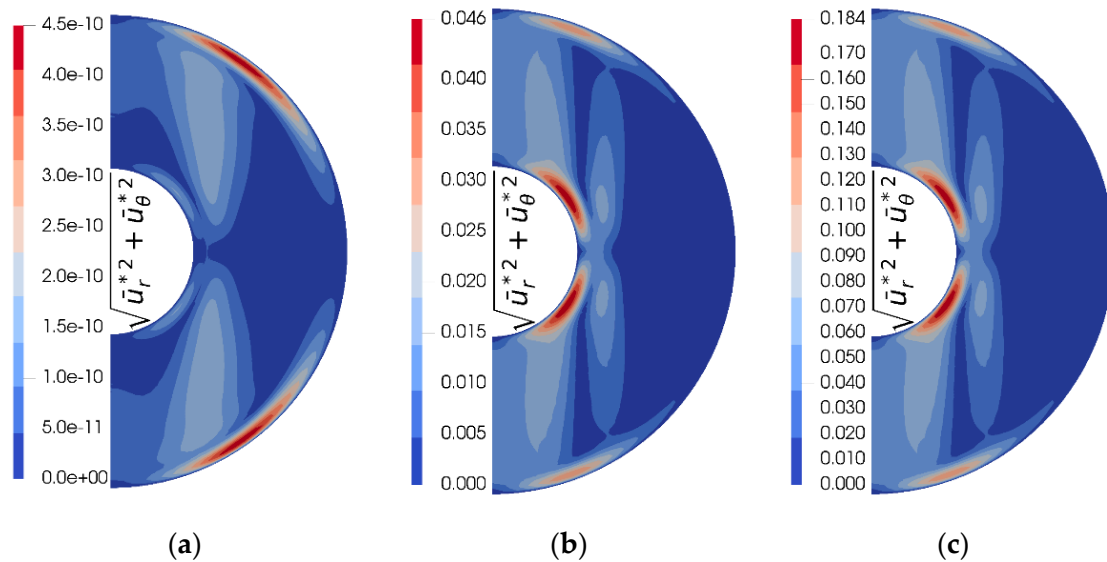

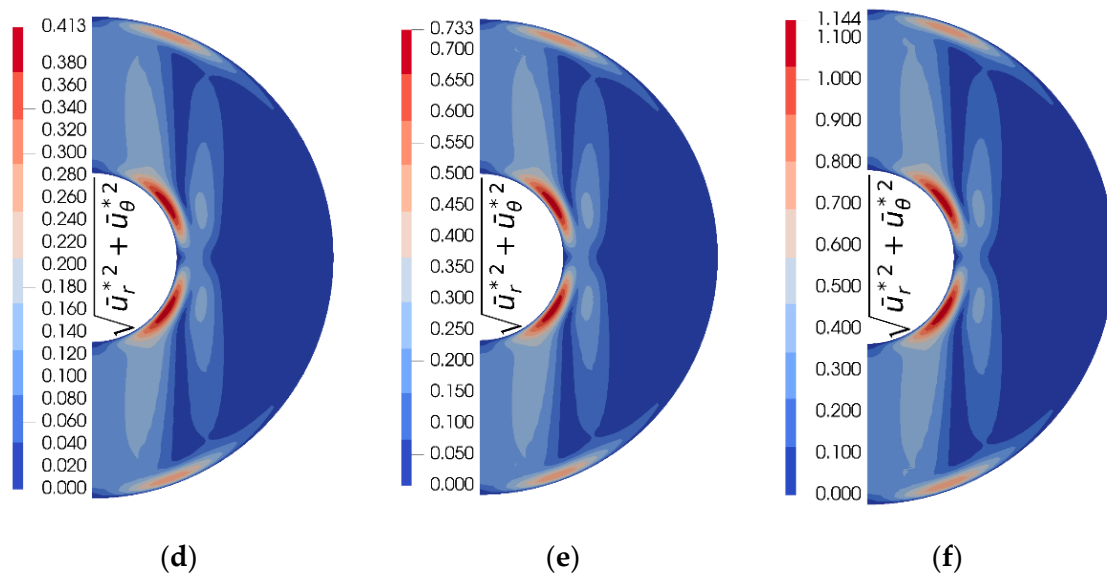(**a**)   (**b**)   (**c**)

Figure 8. *Cont.*

(d)   **(e)**   **(f)**

Figure 8. Contour maps of velocity magnitude of $\sqrt{\overline{u}_r^{*2} + \overline{u}_\theta^{*2}}$ in a meridional cross section at the steady state of $t^* = 1.5$: (**a**) $Fr = 0$; (**b**) $Fr = 0.1$; (**c**) $Fr = 0.2$; (**d**) $Fr = 0.3$; (**e**) $Fr = 0.4$; (**f**) $Fr = 0.5$.

3.3. Linear Stability Analysis

In the present stability analysis, a virtual time-derivative term is introduced to obtain a solution of an eigenvalue problem iteratively, and the most dangerous eigenvalue and its eigenfunction are obtained by a method using both a Red and Black HSMAC method and a Newton method [28–30]. Here, the arbitrary variable F is introduced as follows in order to derive the disturbance equation.

$$F = \overline{F}(r^*, \theta) + F'(r^*, \theta, \phi, t^*) = \overline{F}(r^*, \theta) + \widetilde{F}(r^*, \theta) \exp(s^* t^* + ik\phi) + c.c. \tag{36}$$

$$\widetilde{F} = \widetilde{F}_R + i\widetilde{F}_I \tag{37}$$

where F is an arbitral function, and *c.c.* indicates the complex conjugate of the former term. By substituting Equation (36) into Equations (11)–(15) and subtracting the basic state and ignoring the quadratic quantities, we can derive the linearized disturbance equations. The linearized disturbance equations constitute an eigenvalue problem.

3.3.1. Dimensionless Disturbance Equations

The dimensionless disturbance equations are summarized as follows:
Conservation law of mass:

$$\frac{1}{r^{*2}}\frac{\partial\left(r^{*2}\widetilde{u}_r^*\right)}{\partial r^*} + \frac{1}{r^*\sin\theta}\frac{\partial\left(\widetilde{u}_\theta^*\sin\theta\right)}{\partial\theta} + \frac{ik\widetilde{u}_\phi^*}{r^*\sin\theta} = 0 \tag{38}$$

Momentum equation—radius direction:

$$
\begin{aligned}
s^*\widetilde{u}_r^* + \overline{u}_r^*\frac{\partial\widetilde{u}_r^*}{\partial r^*} + \widetilde{u}_r^*\frac{\partial\overline{u}_r^*}{\partial r^*} + \frac{\overline{u}_\theta^*}{r^*}\frac{\partial\widetilde{u}_r^*}{\partial\theta} + \frac{\widetilde{u}_\theta^*}{r^*}\frac{\partial\overline{u}_r^*}{\partial\theta} + \frac{ik\widetilde{u}_r^*\overline{u}_\phi^*}{r^*\sin\theta} - \frac{2\overline{u}_\theta^*\widetilde{u}_\theta^* + 2\overline{u}_\phi^*\widetilde{u}_\phi^*}{r^*} \\
= -\frac{\partial\widetilde{p}^*}{\partial r^*} + RaPr\widetilde{T}^*r^*\left(\frac{1}{r_{out}^*} - Fr^2\sin^2\theta\right) + \frac{Pr}{Ek}\widetilde{u}_\phi^*\sin\theta \\
+ Pr\left(\nabla^{*2}\widetilde{u}_r^* - \frac{k^2\widetilde{u}_r^*}{r^{*2}\sin\theta} - \frac{2\widetilde{u}_r^*}{r^{*2}} - \frac{2}{r^{*2}}\frac{\partial\widetilde{u}_\theta^*}{\partial\theta} - \frac{2\widetilde{u}_\theta^*\cot\theta}{r^{*2}} - \frac{2ik\widetilde{u}_\phi^*}{r^{*2}\sin\theta}\right)
\end{aligned}
\tag{39}
$$

Momentum equation—poloidal direction:

$$
\begin{aligned}
s^*\widetilde{u}_\theta^* + \overline{u}_r^*\frac{\partial\widetilde{u}_\theta^*}{\partial r^*} + \widetilde{u}_r^*\frac{\partial\overline{u}_\theta^*}{\partial r^*} + \frac{\overline{u}_\theta^*}{r^*}\frac{\partial\widetilde{u}_\theta^*}{\partial\theta} + \frac{\widetilde{u}_\theta^*}{r^*}\frac{\partial\overline{u}_\theta^*}{\partial\theta} + \frac{ik\overline{u}_\phi^*\widetilde{u}_\phi^*}{r^*\sin\theta} + \frac{\overline{u}_r^*\widetilde{u}_\theta^* + \widetilde{u}_r^*\overline{u}_\theta^* - 2\overline{u}_\phi^*\widetilde{u}_\phi^*\cot\theta}{r^*} \\
= -\frac{1}{r^*}\frac{\partial\widetilde{p}^*}{\partial\theta} - RaPrFr^2\widetilde{T}^*r^*\sin\theta\cos\theta + \frac{Pr}{Ek}\widetilde{u}_\phi^*\cos\theta + Pr\left(\nabla^{*2}\widetilde{u}_\theta^* - \frac{\left(k^2+1\right)\widetilde{u}_\theta^*}{r^{*2}\sin^2\theta} + \frac{2}{r^{*2}}\frac{\partial\widetilde{u}_r^*}{\partial\theta} - \frac{2ik\widetilde{u}_\phi^*\cos\theta}{r^{*2}\sin^2\theta}\right)
\end{aligned}
\tag{40}
$$

Momentum equation—toroidal direction:

$$s^*\widetilde{u}_\phi^* + \overline{u}_r^*\frac{\partial \widetilde{u}_\phi^*}{\partial r^*} + \widetilde{u}_r^*\frac{\partial \overline{u}_\phi^*}{\partial r^*} + \frac{\overline{u}_\theta^*}{r^*}\frac{\partial \widetilde{u}_\phi^*}{\partial \theta} + \frac{\widetilde{u}_\theta^*}{r^*}\frac{\partial \overline{u}_\phi^*}{\partial \theta} + \frac{ik\overline{u}_\phi^*\widetilde{u}_\phi^*}{r^*\sin\theta} + \frac{\overline{u}_r^*\widetilde{u}_\phi^* + \widetilde{u}_r^*\overline{u}_\phi^*}{r^*} + \frac{\left(\overline{u}_\phi^*\widetilde{u}_\theta^* + \widetilde{u}_\phi^*\overline{u}_\theta^*\right)\cot\theta}{r^*}$$
$$= -\frac{ik\widetilde{p}^*}{r^*\sin\theta} - \frac{Pr}{Ek}\left(\widetilde{u}_r^*\sin\theta + \widetilde{u}_\theta^*\cos\theta\right) + Pr\left(\nabla^{*2}\widetilde{u}_\phi^* - \frac{(k^2+1)\widetilde{u}_\phi^*}{r^{*2}\sin^2\theta} + \frac{2ik\widetilde{u}_r^*}{r^{*2}\sin\theta} + \frac{2ik\widetilde{u}_\theta^*\cos\theta}{r^{*2}\sin^2\theta}\right) \tag{41}$$

Energy equation:

$$s^*\widetilde{T}^* + \overline{u}_r^*\frac{\partial\widetilde{T}^*}{\partial r^*} + \widetilde{u}_r^*\frac{\partial\overline{T}^*}{\partial r^*} + \frac{\overline{u}_\theta^*}{r^*}\frac{\partial\widetilde{T}^*}{\partial\theta} + \frac{\widetilde{u}_\theta^*}{r^*}\frac{\partial\overline{T}^*}{\partial\theta} + \frac{ik\overline{u}_\phi^*\widetilde{T}^*}{r^*\sin\theta} = \nabla^{*2}\widetilde{T}^* - \frac{k^2\widetilde{T}^*}{r^{*2}\sin^2\theta} \tag{42}$$

3.3.2. Procedure of the Eigenvalue Problem Solution

The procedure of the eigenvalue solution method adopted in this analysis is described. First, the virtual time-derivative term was introduced in the linearized disturbance equations for Equations (39)–(42). Second, the HSMAC method was applied to the equations, and a Newton method was also applied to obtain a complex eigenvalue, where n is the time step and m is the number of iterations of the Newton method.

The virtual time was developed like the calculation of a normal incompressible flow. During that time, the pressure correction formula to satisfy the conservation of mass is given as shown in Equation (43), where the superscript # represents a symbol of the predicted velocity.

$$(\delta\widetilde{p}^*)_{i,j} = -\frac{\frac{1}{r^{*2}}\frac{\partial\left(r^{*2}\widetilde{u}_r^{*\#}\right)}{\partial r^*} + \frac{1}{r^*\sin\theta}\frac{\partial\left(\widetilde{u}_\theta^{*\#}\sin\theta\right)}{\partial\theta} + \frac{ik\widetilde{u}_\phi^{*\#}}{r^*\sin\theta}}{\Delta\tau\left[\frac{2}{(\Delta r^*)^2} + \frac{2}{r^{*2}(\Delta\theta)^2} + \frac{k^2}{r^{*2}\sin^2\theta}\right]} \tag{43}$$

A Newton method was introduced to search for complex eigenvalues that satisfy the linearized disturbance equations during the flow instability analysis. The linearized disturbance equation for the toroidal direction was used to derive the Newton method formula. First, it was decoupled into a real part and an imaginary part as follows:

$$F_R(s_R^*) = -s_R^*\widetilde{u}_\phi^{*\,n}{}_R + s_I^*\widetilde{u}_\phi^{*\,n}{}_I + B_{\phi R}$$
$$F_I(s_I^*) = -s_R^*\widetilde{u}_\phi^{*\,n}{}_I - s_I^*\widetilde{u}_\phi^{*\,n}{}_R + B_{\phi I}$$
$$B_\phi = -\overline{u}_r^*\frac{\partial\widetilde{u}_\phi^*}{\partial r^*} - \widetilde{u}_r^*\frac{\partial\overline{u}_\phi^*}{\partial r^*} - \frac{\overline{u}_\theta^*}{r^*}\frac{\partial\widetilde{u}_\phi^*}{\partial\theta} - \frac{\widetilde{u}_\theta^*}{r^*}\frac{\partial\overline{u}_\phi^*}{\partial\theta} - \frac{ik\overline{u}_\phi^*\widetilde{u}_\phi^*}{r^*\sin\theta} - \frac{\overline{u}_r^*\widetilde{u}_\phi^* + \widetilde{u}_r^*\overline{u}_\phi^*}{r^*} - \frac{\left(\overline{u}_\phi^*\widetilde{u}_\theta^* + \widetilde{u}_\phi^*\overline{u}_\theta^*\right)\cot\theta}{r^*} \tag{44}$$
$$+ \frac{Pr}{Ek}\left(\widetilde{u}_r^*\sin\theta + \widetilde{u}_\theta^*\cos\theta\right) - \frac{ik\widetilde{p}^*}{r^*\sin\theta} + Pr\left[\nabla^{*2}\widetilde{u}_\phi^* - \frac{(k^2+1)\widetilde{u}_\phi^*}{r^{*2}\sin^2\theta} + \frac{2ik\widetilde{u}_r^*}{r^{*2}\sin\theta} + \frac{2ik\widetilde{u}_\theta^*\cos\theta}{r^{*2}\sin^2\theta}\right]$$

The Newton method formula was derived for each of the real part and the imaginary part as defined.

$$\frac{\partial F_R}{\partial s_R^*} = -\widetilde{u}_\phi^{*\,n}{}_R \quad , \quad \frac{\partial F_I}{\partial s_I^*} = -\widetilde{u}_\phi^{*\,n}{}_R \tag{45}$$

From the above, the formula of Newton method for searching the complex eigenvalue is as follows, where C is the coefficient, which is related to the convergence speed for the iteration procedure. In this analysis, it was set that $C_R = C_I = 1.0\times 10^{-3}$.

$$s_R^{*\,m+1} = s_R^{*\,m} - C_R\cdot\frac{F_R(s_R^*)}{\partial F_R/\partial s_R^*} = s_R^{*\,m} + C_R\cdot\frac{\widetilde{u}_\phi^{*\,n+1}{}_R - \widetilde{u}_\phi^{*\,n}{}_R}{\widetilde{u}_\phi^{*\,n}{}_R\Delta\tau}$$
$$s_I^{*\,m+1} = s_I^{*\,m} - C_I\cdot\frac{F_I(s_I^*)}{\partial F_I/\partial s_I^*} = s_I^{*\,m} + C_I\cdot\frac{\widetilde{u}_\phi^{*\,n+1}{}_I - \widetilde{u}_\phi^{*\,n}{}_I}{\widetilde{u}_\phi^{*\,n}{}_R\Delta\tau} \tag{46}$$

While calculating this Newton method, the most dangerous eigenvalue and its corresponding eigenfunction can be obtained by evolving the virtual time and repeating this procedure until both the linear growth rate $S_R{}^*$ and the angular frequency $S_I{}^*$ converge.

3.3.3. Initial Conditions

The initial conditions were set as follows: At least one variable should be set to a non-zero value.

$$\widetilde{T}^*_{R,init} = \widetilde{T}^*_{I,init} = \widetilde{u}^*_{r\,R,init} = \widetilde{u}^*_{r\,I,init} = \widetilde{u}^*_{\theta\,R,init} = \widetilde{u}^*_{\theta\,I,init} = \widetilde{p}^*_{R,init} = \widetilde{p}^*_{I,init} = 0$$
$$\widetilde{u}^*_{\phi R,init} = 1 \quad , \quad \widetilde{u}^*_{\phi I,init} = 0 \tag{47}$$

3.3.4. Boundary Conditions

The boundary conditions at the inner and outer walls are set as follows:

$$\widetilde{T}^* = 0 \quad , \quad \widetilde{u}^*_r = \widetilde{u}^*_\theta = \widetilde{u}^*_\phi = 0 \quad , \quad \frac{\partial \widetilde{p}^*}{\partial r^*} = 0 \qquad at \quad r^* = r^*_{in} \tag{48}$$

$$\widetilde{T}^* = 0 \quad , \quad \widetilde{u}^*_r = \widetilde{u}^*_\theta = \widetilde{u}^*_\phi = 0 \quad , \quad \frac{\partial \widetilde{p}^*}{\partial r^*} = 0 \qquad at \quad r^* = r^*_{out} \tag{49}$$

whereas those at the axis of rotation are as follows:

$$\frac{\partial \widetilde{T}^*}{\partial \theta} = \frac{\partial \widetilde{u}^*_r}{\partial \theta} = \widetilde{u}^*_\theta = \widetilde{u}^*_\phi = \frac{\partial \widetilde{p}^*}{\partial \theta} = 0 \qquad at \quad \theta = 0, \pi \tag{50}$$

3.4. Results

3.4.1. Linear Growth Rate and Phase Speed

Figure 9 shows the linear growth rate and phase speed obtained by the linear stability analysis. The definition of the phase speed V^{LSA}_{ps} is shown in Equation (51).

$$V^{LSA}_{ps} = -\frac{s^*_I}{k} \tag{51}$$

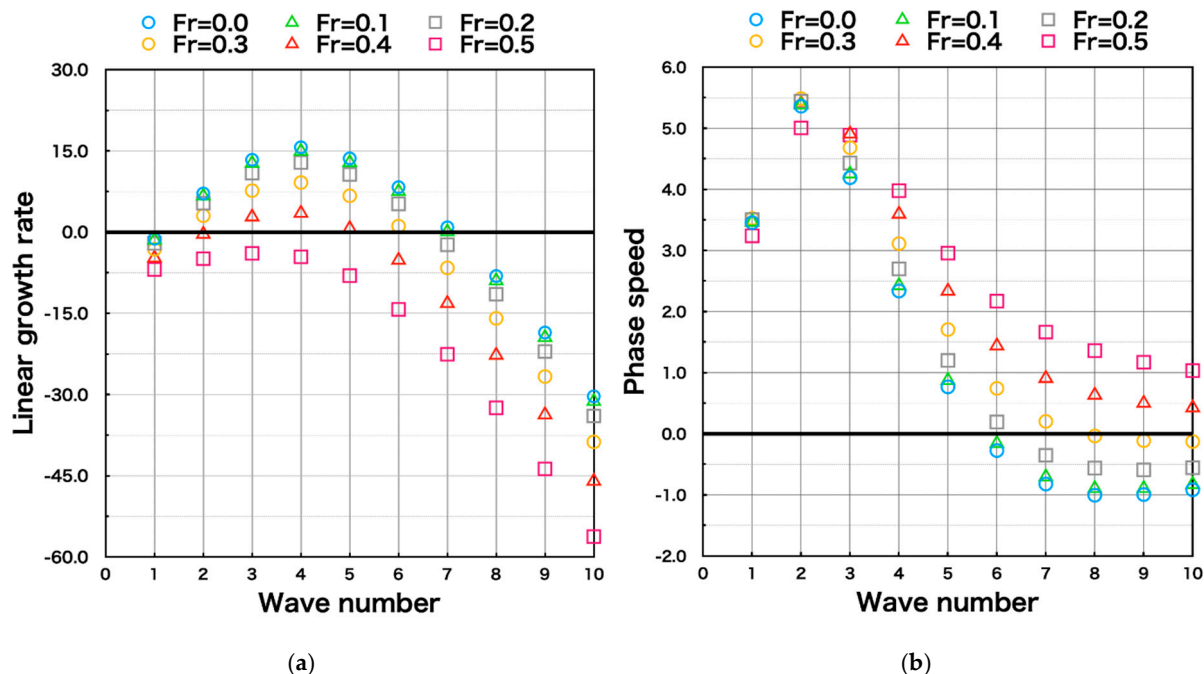(**a**)   (**b**)

Figure 9. Influences of the Froude number on the linear growth rate and the phase speed. The non-dimensional parameters used in the linear stability analyses are the same as in the previous numerical simulations and are shown in Table 1: (**a**) linear growth rate of disturbance; (**b**) phase speed of disturbance.

Figure 9a shows as a general tendency that the higher the Froude number becomes, the lower the linear growth rate is. That is, the larger the influence of centrifugal force is,

the more stable the flow field becomes. Therefore, according to the linear stability theory, the effect of the centrifugal force has the effect of controlling a disturbance of flow. All of the wavenumbers at $Fr = 0.5$ take negative values of the linear growth rate. So, it is considered that the critical Froude number exists between $Fr = 0.4$ and 0.5. Figure 9b shows the wavenumber dependence of the phase speed. The phase speed takes various values depending on the value of the Froude number, but it can be seen that the phase speed takes a positive value regardless of the Froude number near wavenumber 4 where the linear growth rate is positive.

3.4.2. Visualization of Eigenfunction (Two-Dimensional)

Figures 10–12 show the contour map of the real part of eigenfunctions of temperature, pressure and velocity magnitude, respectively, obtained by the present linear stability analyses. The wavenumber of these visualizations is four where the maximum linear growth rate takes place. We focused on the dependency of the Froude number on linear stability of the thermal convection within a spherical shell by changing the effect of centrifugal force.
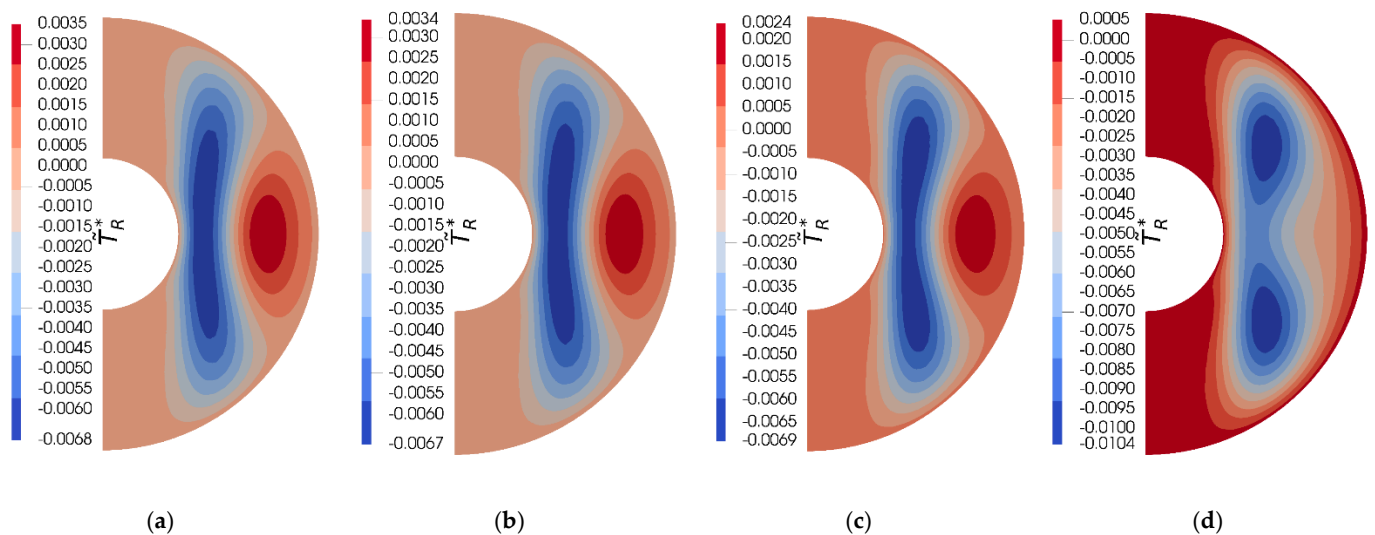
Figure 10. Disturbance of temperature at wavenumber $k = 4$: (**a**) $Fr = 0.0$; (**b**) $Fr = 0.1$; (**c**) $Fr = 0.3$; (**d**) $Fr = 0.5$.
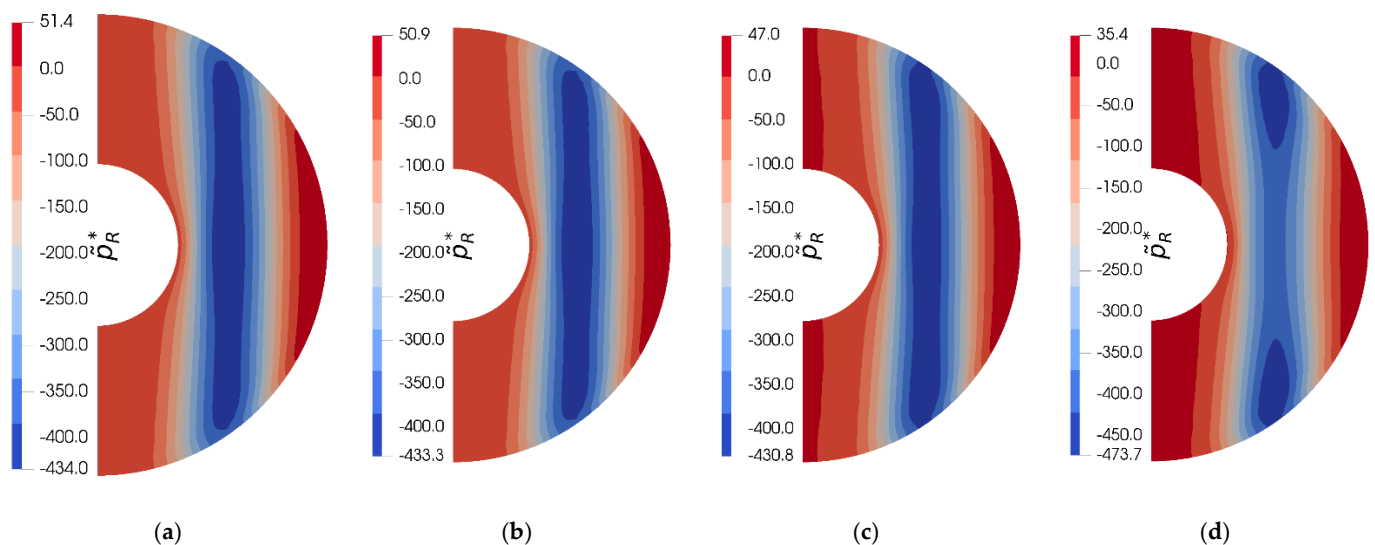
Figure 11. Disturbance of pressure at wavenumber $k = 4$: (**a**) $Fr = 0.0$; (**b**) $Fr = 0.1$; (**c**) $Fr = 0.3$; (**d**) $Fr = 0.5$.
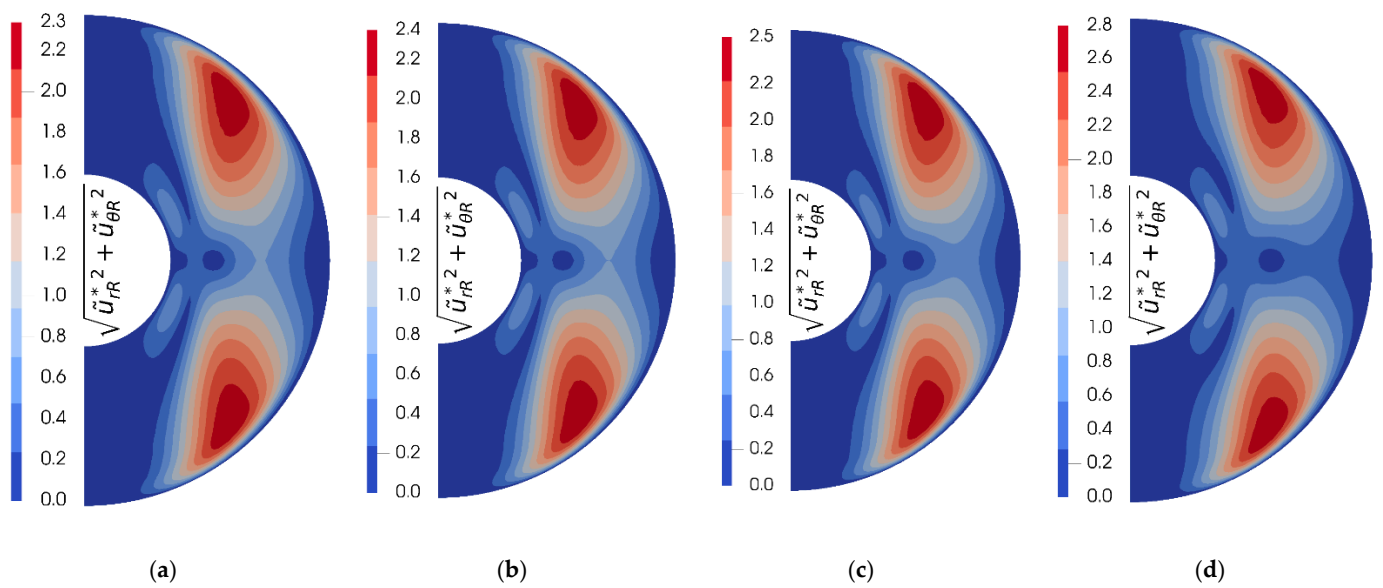
Figure 12. Disturbance of velocity magnitude at wavenumber $k = 4$. The colored contour map indicates $\sqrt{\tilde{u}_r^{*2} + \tilde{u}_\theta^{*2}}$: (**a**) $Fr = 0.0$; (**b**) $Fr = 0.1$; (**c**) $Fr = 0.3$; (**d**) $Fr = 0.5$.

4. Three-Dimensional Numerical Simulation Versus Linear Stability Analysis (LSA)

4.1. Linear Growth Rate

4.1.1. Estimation of Linear Growth Rate from the Result of the Simulation

The linear growth rate in the three-dimensional numerical simulation was estimated from the time change rate of kinetic energy in Figure 4, that is, the slope of a straight line.

4.1.2. Comparison of the Linear Growth Rate

Table 5 shows the linear growth rates for the various values of the Froude number obtained by both the linear stability analysis and the three-dimensional numerical simulation. Since a 3D numerical simulation can include the interaction among several wavenumbers, the comparison between the LSA and the 3D calculation should be made for just above the critical condition. In the present LSA analysis, the most suitable case for such comparison would be the case of $Fr = 0.4$ in which only the three wavenumbers are positive. However, in this analysis of $Fr = 0.4$, the largest linear growth rate obtained by the linear stability analysis ($k = 4$) did not agree with that obtained by the 3D calculation. It was considered that disturbances of the various wavenumbers interacted with each other in the 3D flow field. From a qualitative viewpoint, the tendency that the linear growth rate decreases as the Froude number increases in both LSA and 3D is confirmed.

Table 5. Linear growth rate obtained from the LSA and the 3D simulation for various wavenumbers k and the Froude number Fr. The time ranges in parentheses refer to linear growth periods.

Fr	LSA						3D
	$k = 2$	$k = 3$	$k = 4$	$k = 5$	$k = 6$	$k = 7$	
0.0	7.1385	13.3544	15.6605	13.6097	8.2959	0.8805	14.02 ($t^* = 0.10{\sim}0.60$)
0.1	6.6952	12.7496	14.9745	12.8846	7.5418	0.0927	13.02 ($t^* = 0.50{\sim}0.68$)
0.2	5.3444	10.8951	12.8632	10.6486	5.2151	−2.3352	10.04 ($t^* = 0.70{\sim}0.85$)
0.3	3.0236	7.6642	9.1550	6.7067	1.1102	−6.6116	6.309 ($t^* = 1.10{\sim}1.25$)
0.4	−0.3660	2.8278	3.5230	0.6865	−5.1648	−13.1332	1.935 ($t^* = 2.90{\sim}3.15$)
0.5	−4.9089	−3.9250	−4.5684	−8.0472	−14.2745	−22.5659	-

4.2. Phase Speed

4.2.1. Estimation of the Phase Speed from the Result of the Simulation

Figure 13 shows how the phase speed was estimated from the result of the 3D simulation. As an example, the toroidal velocity at the location of $(r_{in}^* + r_{out}^*)/2$ and $\theta = \pi/2$ for several time instants during the time stage that the toroidal velocity amplified exponentially is shown as a function of toroidal position for the case of $Fr = 0.2$.
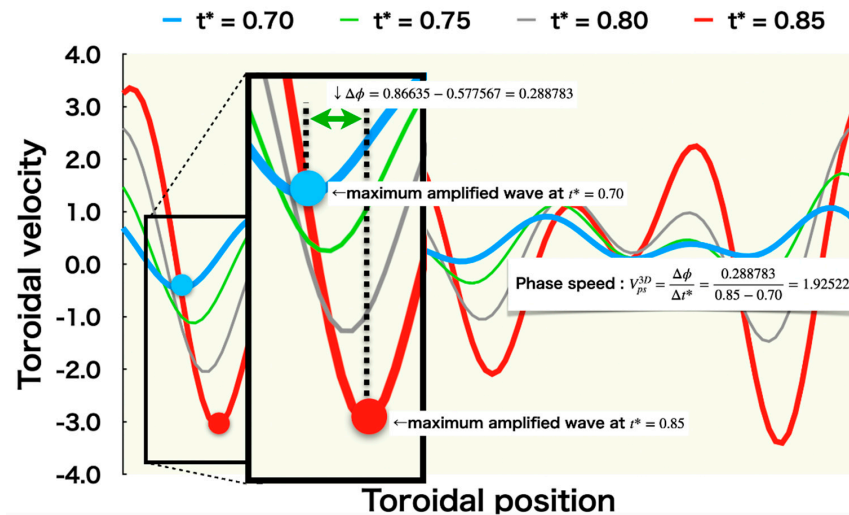

Figure 13. Method of estimating a phase speed from a wave shape obtained by the three-dimensional numerical simulation.

4.2.2. Comparison of the Phase Speed

Table 6 shows the result of phase speeds for each Froude number obtained by the three-dimensional numerical simulation and the linear stability analysis. From a quantitative viewpoint, the result of the linear stability analysis did not agree well with that of the three-dimensional numerical simulation, whereas the direction of the phase speed at the maximum linear growth rate was consistent. For the linear stability analysis, the larger the effect of centrifugal force is, the larger the phase speed is. However, the result of three-dimensional numerical simulation was not this trend. In addition, we can verify that the result of the linear stability analysis almost agreed with the result of the three-dimensional numerical simulation near the critical condition for $Fr = 0.4$.

Table 6. Phase speed for various wavenumbers k and the Froude number Fr.

Fr	LSA						3D
	$k = 2$	$k = 3$	$k = 4$	$k = 5$	$k = 6$	$k = 7$	
0.0.	5.3597	4.1885	2.3341	0.7652	−0.2768	−0.8246	1.733
0.1	5.3834	4.2516	2.4269	0.8752	−0.15	−0.7050	1.733
0.2	5.4402	4.4291	2.6959	1.1969	0.1901	−0.3545	1.925
0.3	5.4820	4.6790	3.1095	1.7031	0.7405	0.2001	5.006
0.4	5.4065	4.9061	3.5951	2.3347	1.4391	0.9074	3.696
0.5	5.0029	4.8861	3.9757	2.9538	2.1684	1.6621	−

4.3. Distribution of Disturbances

Expansion of the Distributions of the Eigenfunction to Three-Dimensional Distributions

The two-dimensional distributions of the eigenfunction obtained by the linear stability analysis can be expanded into the toroidal direction assuming cyclic periodicity using Equation (52).

$$\widetilde{F}^* = \left[\widetilde{F}_R^* \cos(s_I^* t^* + k\phi) - \widetilde{F}_I^* \sin(s_I^* t^* + k\phi) \right] \exp(s_R^* t^*) \tag{52}$$

When we visualize the distribution of disturbances, we do not consider the linear growth rate and phase speed because we focus only on the distributions of disturbances. That is, we calculate Equation (52) on a condition of $t* = 0.0$ and visualize the numerical results. In addition, we visualize the distributions of the disturbances obtained by the three-dimensional numerical simulation by calculating Equation (53).

$$F^{*'} = F^* - \overline{F}^* \tag{53}$$

In this study, we compared distributions of disturbances by both three-dimensional numerical simulation and linear stability analysis for $Fr = 0.2$. First, Figure 14 shows the comparison of the equatorial cross-sectional distribution for the temperature disturbance obtained by Figure 14a three-dimensional simulation and Figure 14b–g linear stability analysis. Second, the same comparison for the toroidal velocity disturbance is shown in Figure 15. The result of visualization by the three-dimensional numerical simulation, the distribution of temperature and toroidal disturbances at the dimensionless time $t* = 0.75$ that the kinetic energy and toroidal velocity field amplified exponentially is shown. According to these figures, we can verify that the influences of disturbances that have a wavenumber of maximum linear growth rate appear on the three-dimensional flow field.
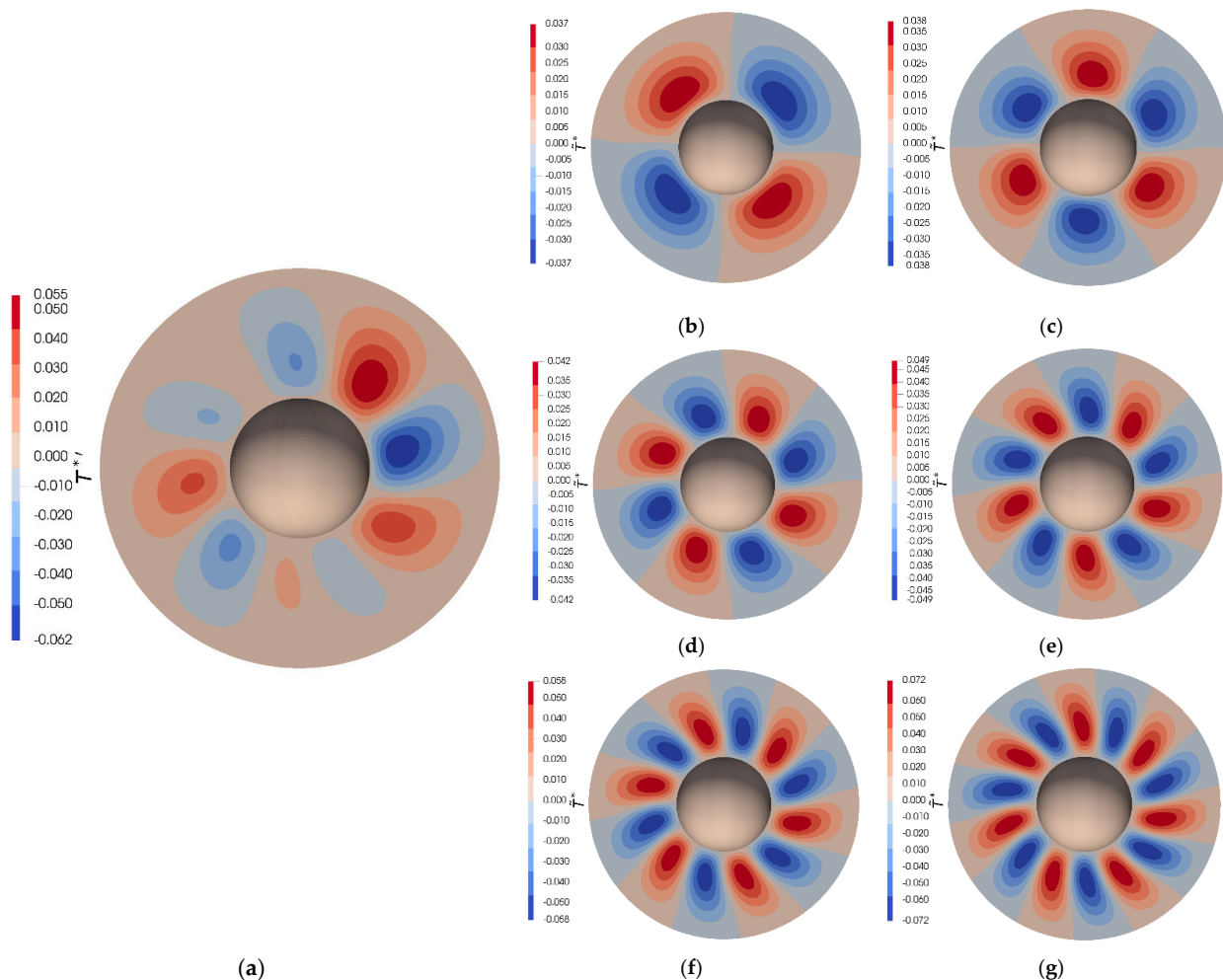

Figure 14. Equatorial cross-sectional distribution of temperature disturbance field for $Fr = 0.2$: (**a**) three-dimensional simulation ($t* = 0.75$); (**b**) LSA ($k = 2$); (**c**) LSA ($k = 3$); (**d**) LSA ($k = 4$); (**e**) LSA ($k = 5$); (**f**) LSA ($k = 6$); (**g**) LSA ($k = 7$).
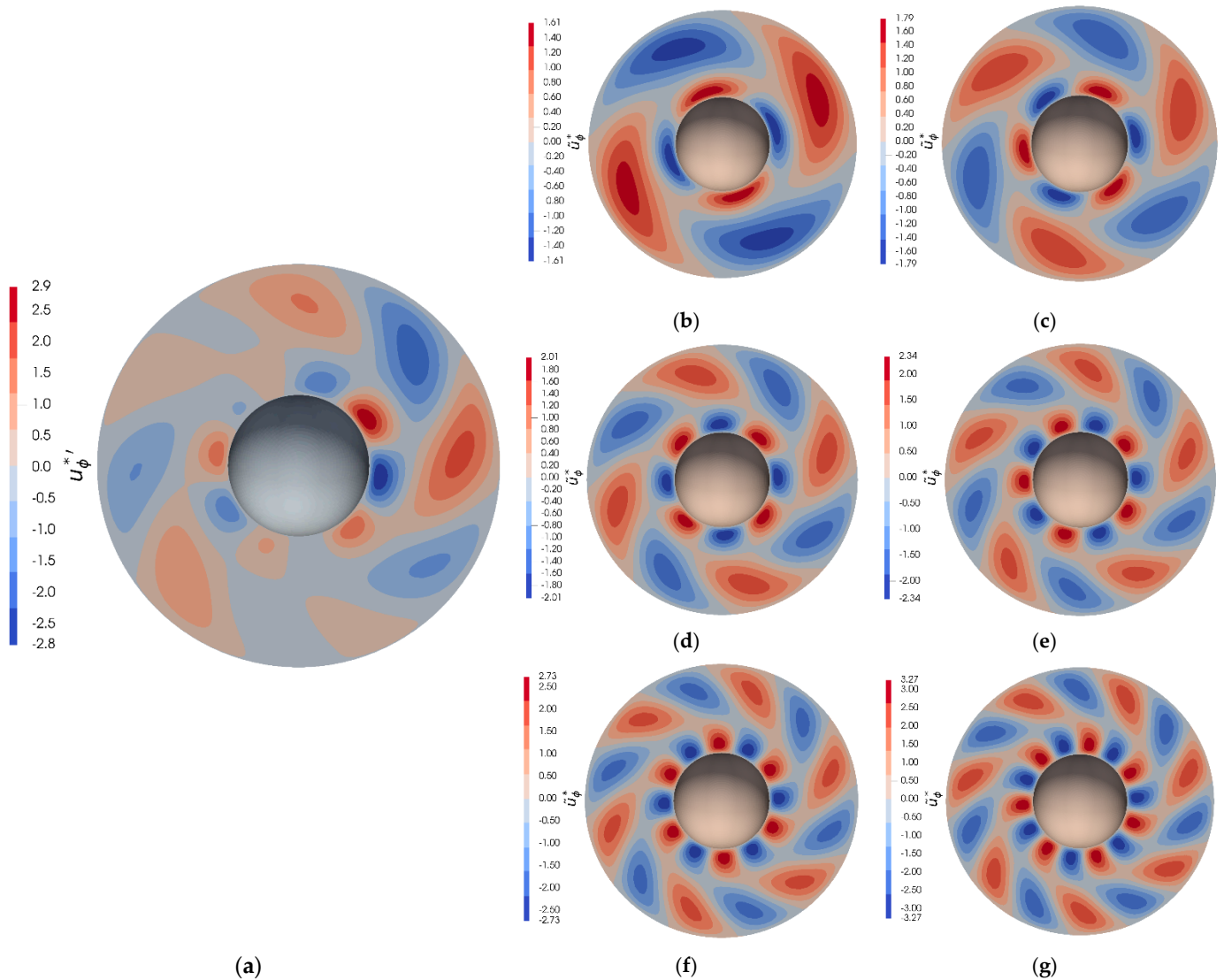
Figure 15. Equatorial cross-sectional distribution of toroidal velocity disturbance field for $Fr = 0.2$: (**a**) three-dimensional simulation ($t^* = 0.75$); (**b**) LSA ($k = 2$); (**c**) LSA ($k = 3$); (**d**) LSA ($k = 4$); (**e**) LSA ($k = 5$); (**f**) LSA ($k = 6$); (**g**) LSA ($k = 7$).

Figure 15 shows that the wavenumber of disturbance is between three and five. According to the linear stability analysis, these wavenumbers have large linear growth rates. So, we consider that the influences of disturbances of a large linear growth rate appear even in the three-dimensional flow field.

We defined the second invariant of the velocity gradient that we called the Q value as shown in Equation (54).

$$
\begin{aligned}
Q^* = &-\frac{1}{r^*}\frac{\partial u_r^*}{\partial r^*}\frac{\partial u_\theta^*}{\partial \theta} - \frac{u_r^*}{r^*}\frac{\partial u_r^*}{\partial r^*} - \frac{1}{r^{*2}\sin\theta}\frac{\partial u_\theta^*}{\partial \theta}\frac{\partial u_\phi^*}{\partial \phi} - \frac{u_r^*}{r^{*2}}\frac{\partial u_\theta^*}{\partial \theta} - \frac{u_\theta^*\cos\theta}{r^{*2}\sin\theta}\frac{\partial u_\theta^*}{\partial \theta} - \frac{u_r^*}{r^{*2}\sin\theta}\frac{\partial u_\phi^*}{\partial \phi} - \frac{u_r^{*2}}{r^{*2}} - \frac{u_r^* u_\theta^*\cos\theta}{r^{*2}\sin\theta} \\
&-\frac{1}{r^*\sin\theta}\frac{\partial u_\phi^*}{\partial \phi}\frac{\partial u_r^*}{\partial r^*} - \frac{u_r^*}{r^*}\frac{\partial u_r^*}{\partial r^*} - \frac{u_\theta^*\cos\theta}{r^*\sin\theta}\frac{\partial u_r^*}{\partial r^*} + \frac{1}{r^*}\frac{\partial u_\theta^*}{\partial r^*}\frac{\partial u_r^*}{\partial \theta} - \frac{u_\theta^*}{r^*}\frac{\partial u_\theta^*}{\partial r^*} + \frac{1}{r^*\sin\theta}\frac{\partial u_\phi^*}{\partial r^*}\frac{\partial u_r^*}{\partial \phi} - \frac{u_\phi^*}{r^*}\frac{\partial u_\phi^*}{\partial r^*} \\
&+\frac{Pr}{2Ek}\frac{1}{r^*}\frac{\partial u_r^*}{\partial \phi} - \frac{Pr}{2Ek}\frac{u_\phi^*\sin\theta}{r^*} + \frac{1}{r^{*2}\sin\theta}\frac{\partial u_\phi^*}{\partial \theta}\frac{\partial u_\theta^*}{\partial \phi} - \frac{u_\phi^*\cot\theta}{r^{*2}}\frac{\partial u_\phi^*}{\partial \theta} + \frac{Pr}{2Ek}\frac{\cos\theta}{r^*\sin\theta}\frac{\partial u_\theta^*}{\partial \phi} - \frac{Pr}{2Ek}\frac{u_\phi^*\cos^2\theta}{r^*\sin\theta}
\end{aligned}
\tag{54}
$$

Figure 16a,b show a perspective view of the thermal convection structure in the spherical shell for both the three-dimensional simulation at an exponentially growing stage and the linear stability analysis. Figure 16c,d show an equatorial cross-sectional distribution of the Q value of disturbance by the three-dimensional simulation at $t^* = 0.75$ and linear stability analysis ($k = 4$). According to Figure 16a,b, we can confirm that a

quasi-uniform flow structure forms along the rotating axis. From the visualization result of this 3D simulation, it is confirmed that the structure of five wavenumbers is generated, although the iso-surface of the Q value is not perfectly symmetric with respect to the rotating axis. This disagrees with the wavenumber that takes its maximum linear growth rate obtained by the linear stability analysis.
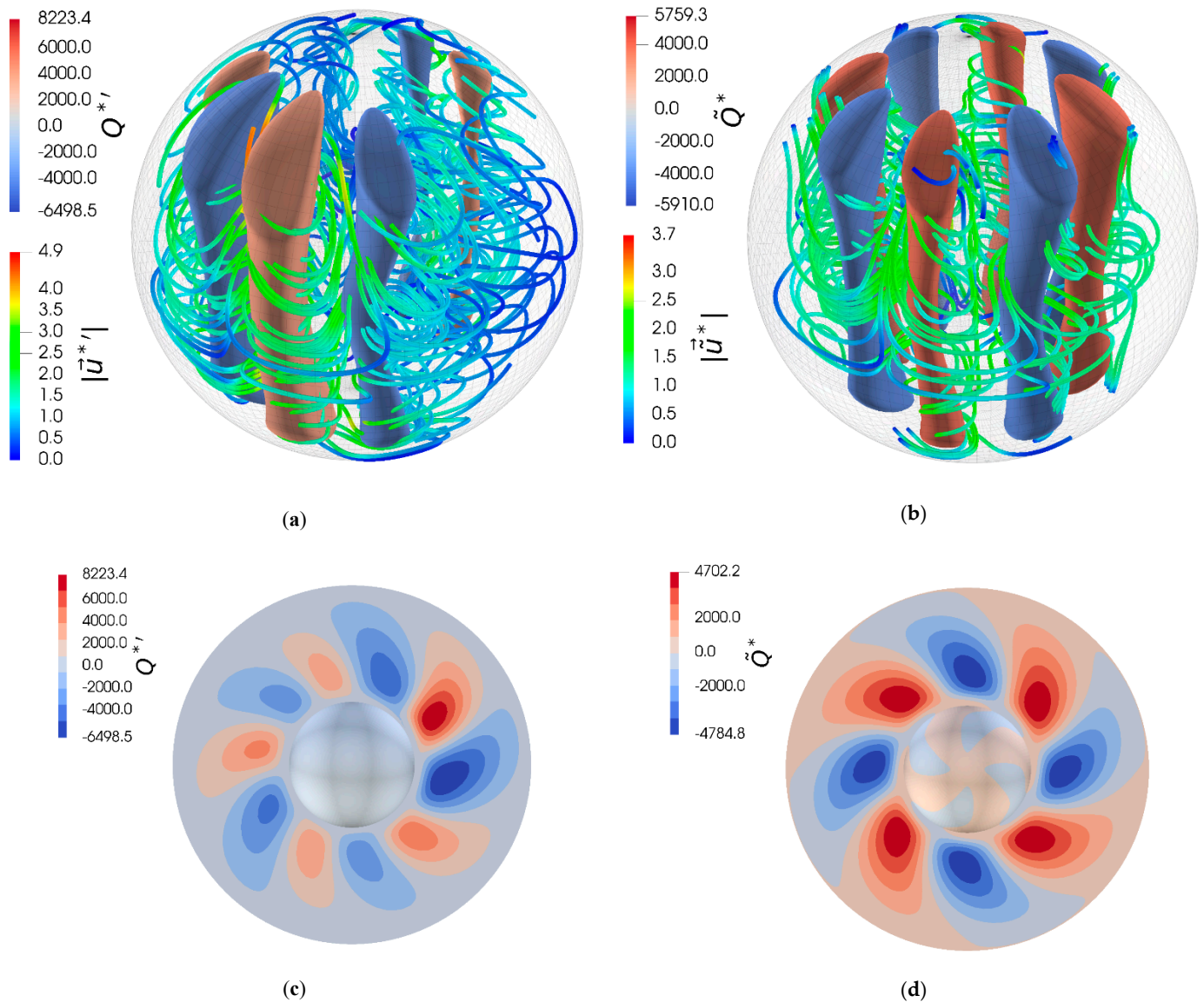

(a)

(b)

(c)

(d)

Figure 16. Thermal convection structure of disturbances for $Fr = 0.2$. The blue and red iso-surfaces indicate the two Q values selected, while the colored lines indicate the stream line: (**a**) three-dimensional numerical simulation ($Q^{*'} = \pm 4000.0$) at $t^* = 0.75$; (**b**) linear stability analysis ($k = 4$) ($\widetilde{Q}^* = \pm 4000.0$); (**c**) equatorial cross-sectional distribution of the Q value of disturbance by the three-dimensional simulation at $t^* = 0.75$; (**d**) equatorial cross-sectional distribution of the Q value of disturbance by the linear stability analysis. ($k = 4$).

As the Froude number becomes smaller, various wavenumbers with positive linear growth rate increase. Therefore, the wavenumber appearing in the flow field is not necessarily limited to the wavenumber with the maximum linear growth rate. However, the result of wavenumber 5 obtained by the 3D simulation suggests that the linear stability theory is not completely useless because the value of Sr at wavenumber 5 obtained by LSA is rather large as shown in Figure 9a.

5. Discussion

5.1. About a Flat Region of Time Evolution of Kinetic Energy

According to the time evolution of kinetic energy shown in Figure 4a, only for $Fr = 0$, can it be recognized that the disturbance grows linearly from the point around 10^{-7} on the vertical axis immediately after the start of the calculation. On the other hand, in cases other than $Fr = 0$, the growth of the disturbance is visible after passing a flat period that depends on the value of the Froude number. We believe that the steady growth of disturbances is hidden during this flat period (axisymmetric basic flow) because the order of magnitude of disturbances is much smaller than the kinetic energy of the basic state. The time delay before the linear growth of disturbances appears can be explained in this way.

5.2. About the Flow Field for Fr = 0.4

We discussed the near critical state of $Fr = 0.4$ to compare the three-dimensional simulation with the linear stability analysis. Figure 17 shows the temporal fluctuation of the kinetic energy until a dimensionless time 5.0 as shown in (a), and the equatorial cross-sectional distributions of toroidal velocity field at the dimensionless time 5.0 as shown in (b). According to Figure 17a, the time that the kinetic energy amplified exponentially is delayed for this case of near the critical state compared to other low Froude numbers. Figure 17b shows that the wavenumber of appearing on the three-dimensional flow field is four.
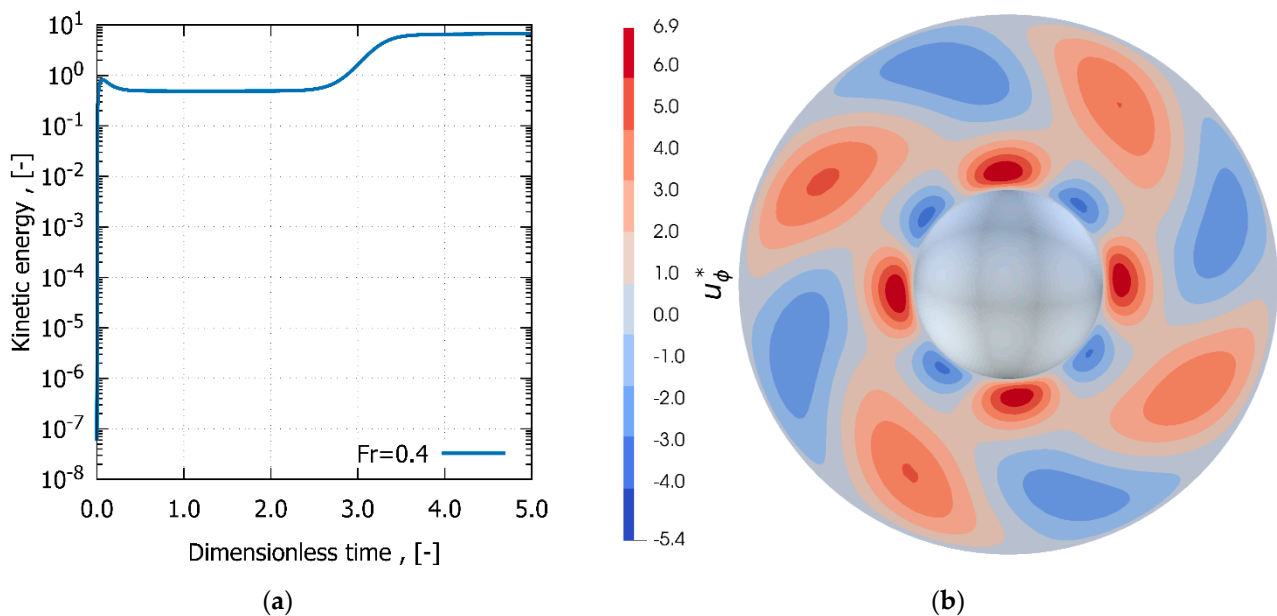

(a) (b)

Figure 17. Results of the three-dimensional simulation for $Fr = 0.4$: (**a**) temporal evolution of the kinetic energy; (**b**) the equatorial cross-sectional distribution of toroidal velocity field at $t^* = 5.0$.

Figure 18a shows the equatorial cross-sectional distribution of toroidal velocity disturbance at the dimensionless time 3.0 that the flow field amplified exponentially for $Fr = 0.4$. The strength of the velocity is not uniform along the toroidal direction. However, the wavenumber and its shape appearing in this growing stage agree well with the corresponding LSA solution shown in Figure 18b.
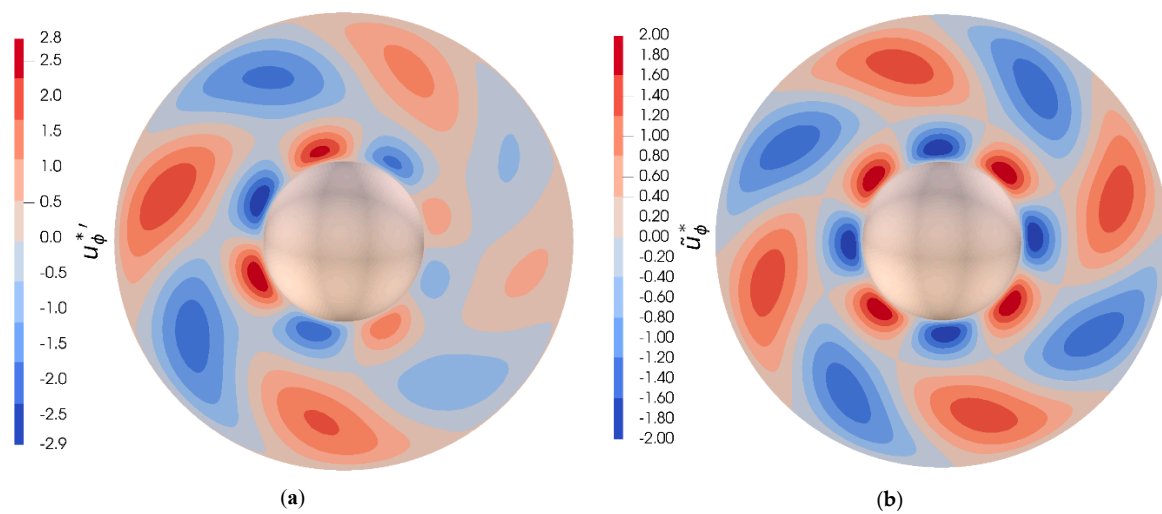
Figure 18. The equatorial cross-sectional disturbance of toroidal velocity field for *Fr* = 0.4: (**a**) three-dimensional simulation at *t** = 3.0 (a stage of exponentially growing); (**b**) linear stability analysis (*k* = 4).

5.3. About the Three-Dimensional Flow Field and Disturbances of the Maximum Linear Growth Rate on the Quasi-Steady State

We compared the result of *Fr* = 0.1 with *Fr* = 0.4 about the time fluctuation of the equatorial cross-sectional distribution of the *Q* value at the quasi-steady state after it was amplified exponentially. The evaluating point of the comparison is the wavenumber by three-dimensional simulation and linear stability analysis. Figure 19a–c show the results by the three-dimensional simulation, and Figure 19d is the result by the linear stability analysis. About the linear stability analysis at *Fr* = 0.1, the wavenumbers of the positive linear growth rate are observed from two to seven, especially the wavenumbers between three to five have relatively large linear growth rates. We can verify the wavenumber by the three-dimensional simulation. Figure 19a shows that the wavenumber is four or five. Figure 19b shows that the wavenumber is three or four. Figure 19c shows that the wavenumber is three. We consider that a characteristic of the disturbance amplified exponentially remains until the large nonlinear effect becomes significant because the wavenumber obtained by the 3D simulation is nearly the same as that of the maximum linear growth rate obtained by the LSA.
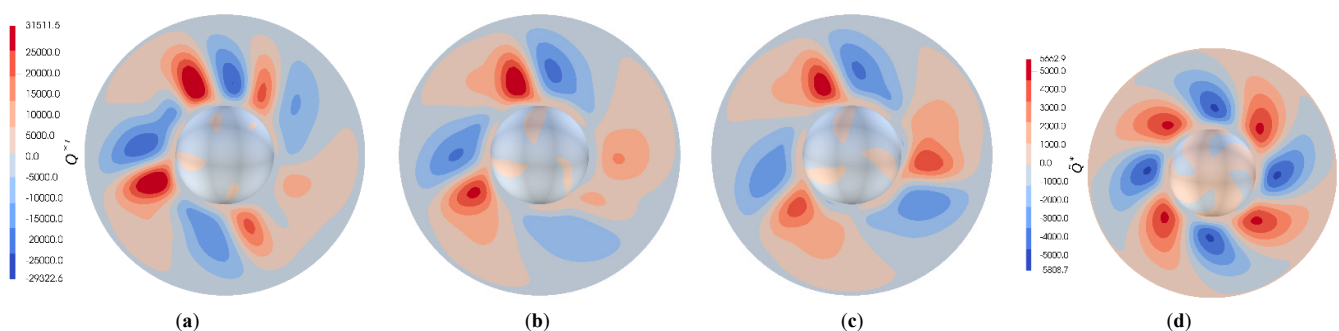

Figure 19. The equatorial cross-sectional distribution of the second invariant of the disturbance velocity gradient field at several time instants for *Fr* = 0.1: (**a**) *t** = 1.5; (**b**) *t** = 1.75; (**c**) *t** = 2.0; (**d**) linear stability analysis (*k* = 4).

Figure 20a–c show the results by the three-dimensional simulation and Figure 20d is the result by the linear stability analysis (*k* = 4). According to Figure 20, the wavenumber obtained by the 3D simulation is about 4 regardless of the time, which is in good agreement with the wavenumber 4 predicted by the linear stability analysis. This is due to the fact that

the growth rate for *Fr* = 0.4 takes some small positive values. In other words, it is considered that the influence of the nonlinear effect on the flow obtained by the three-dimensional simulation is small.
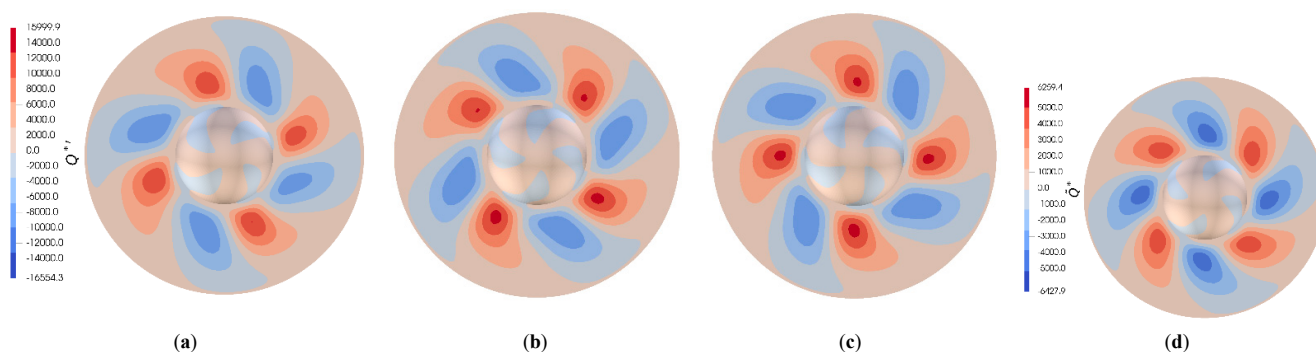

Figure 20. The equatorial cross-sectional distribution of the second invariant of the disturbance velocity gradient field for *Fr* = 0.4: (**a**) *t** = 3.5; (**b**) *t** = 4.25; (**c**) *t** = 5.0; (**d**) linear stability analysis (*k* = 4).

6. Conclusions

In this study, a three-dimensional numerical simulation and a linear stability analysis were performed for thermal convection in a rotating spherical shell. In particular, we focused on the effect of centrifugal buoyancy on the transition from an axisymmetric flow to a flow with a wavenumber in the toroidal direction. Our study reached the following conclusions:

1. Considering the centrifugal buoyancy, weak convection takes place even in the basic state in which an axisymmetric flow field is assumed. In cases other than *Fr* = 0, the growth of the disturbance is visible after passing a flat period. The steady growth of disturbances is hidden during this flat period in which axisymmetric basic flow prevails.
2. In the case of *Fr* = 0.4 that is near the critical Froude number, from a quantitative viewpoint, the largest linear growth rate from the linear stability analysis is not in good agreement with that from the three-dimensional simulation. However, on a qualitative viewpoint, the wavenumber and the direction of phase speed obtained by the three-dimensional simulation are in good agreement with those from the linear stability analysis.
3. It was found that the greater the influence of centrifugal buoyancy, the less unstable the convection becomes.

As a future study, we would like to investigate the influence of the magnetohydro-dynamics effect, such as an applied magnetic field or an induction magnetic field, to obtain a new basic knowledge for elucidating the mechanism of generating and preserving the geomagnetism.

Nomenclature

Ek	Ekman number (-)
E_{kin}	dimensionless kinetic energy (-)
$\boldsymbol{e}_r$	unit vector in radial direction (-)
$\boldsymbol{e}_z$	unit vector in axial direction (-)
$\boldsymbol{e}_\theta$	unit vector in poloidal direction (-)
$\boldsymbol{e}_\varphi$	unit vector in toroidal direction (-)
F	function or arbitral variable (-)
Fr	Froude number (-)
g_0	gravitational acceleration at r_{out} (m/s^2)
i	imaginary unit (-)
k	azimuthal wavenumber (-)
N	number of grids (-)
p	pressure (Pa)
p_s	static pressure (Pa)
Pr	Prandtl number (-)
Q*	second invariant of the velocity gradient (-)
$\boldsymbol{r}$	position vector (m)
r	radial coordinate (m)
r_0	characteristic length = $r_{out} - r_{in}$ (m)
r_{in}	inner radius (m)
r_{out}	outer radius (m)
Ra	Rayleigh number (-)
s	complex eigenvalue (rad/s)
t	time (s)
T	temperature (K)
T_c	temperature at cold wall (K)
T_h	temperature at hot wall (K)
T_0	reference temperature = $(T_h + T_c)/2$ (K)
$\boldsymbol{u}$	velocity vector (m/s)
V	volume of spherical shell (m^3)
V_{ps}	phase speed (m/s)
Greek symbols	
α	thermal diffusivity (m^2/s)
β_0	volumetric coefficient of thermal expansion at T_0 (1/K)
η	radius ratio (-)
θ	poloidal coordinate (-)
μ	viscosity (Pa s)
ν	kinematic viscosity = μ/ρ_0 (m^2/s)
φ	toroidal coordinate (-)
ρ	density (kg/m^3)
ρ_0	density at T_0 (kg/m^3)
Ω	angular velocity (rad/s)
$\boldsymbol{\Omega}$	angular velocity vector (rad/s)
Subscripts or superscripts	
*	dimensionless
	basic state
~	amplitude function
I	imaginary part
init	initial value
n	number of iterative steps
r	radial component
R	rotating frame, real part
S	stationary frame
θ	poloidal component
φ	toroidal component

References

1. Chandrasekar, S. *Hydrodynamic and Hydromagnetic Stability*; Dover Publication, Inc.: New York, NY, USA, 1961.
2. Glatzmaier, G.A.; Roberts, P.H. A three-dimensional convective dynamo solution with rotating and finitely conducting inner core and mantle. *Phys. Earth Planet. Inter.* **1995**, *91*, 63–75. [CrossRef]
3. Kono, M.; Roberts, P.H. Definition of the Rayleigh number for geodynamo simulation. *Phys. Earth Planet. Inter.* **2001**, *128*, 13–24. [CrossRef]
4. Kono, M.; Roberts, P.H. Recent geodynamo simulations and observations of the geomagnetic field. *Rev. Geophys.* **2002**, *40*, 4–10. [CrossRef]
5. Busse, F.H. Convective flows in rapidly rotating spheres and their dynamo action. *Phys. Fluids* **2002**, *14*, 1301–1314. [CrossRef]
6. Christensen, U.R.; Aubert, J.; Cardin, P.; Dormy, E.; Gibbons, S.; Glatzmaier, G.A.; Grote, E.; Honkura, Y.; Jones, D.; Kono, M.; et al. A numerical dynamo benchmark. *Phys. Earth Planet. Inter.* **2001**, *128*, 25–34. [CrossRef]
7. Jones, C.A.; Kuzanyan, K.M.; Mitchell, R.H. Linear theory of compressible convection in rapidly rotating spherical shells, using the anelastic approximation. *J. Fluid Mech.* **2009**, *634*, 291–319. [CrossRef]
8. Liu, S.; Wan, Z.H.; Yan, R.; Sun, C.; Sun, D.J. Onset of fully compressible convection in a rapidly rotating spherical shell. *J. Fluid Mech.* **2019**, *873*, 1090–1115. [CrossRef]
9. Kameyama, M. Linear analysis on the onset of thermal convection of highly compressible fluids with variable viscosity and thermal conductivity in spherical geometry: Implications for the mantle convection of super-Earths. *Earth Planets Space* **2021**, *73*, 1–17. [CrossRef]
10. Dormy, E.; Soward, A.M.; Jones, C.A.; Jault, D.; Cardin, P. The onset of thermal convection in rotating spherical shells. *J. Fluid Mech.* **2004**, *501*, 43–70. [CrossRef]
11. Avila, R.; Cabello-González, A.; Ramos, E. A linear stability analysis of thermal convection in spherical shells with variable radial gravity based on the Tau-Chebyshev method. *Int. J. Heat Fluid Flow* **2013**, *44*, 495–508. [CrossRef]
12. Yu, H.; Wang, S. Unified Linear Stability Analysis for Thermal Convections in Spherical Shells Under Different Boundary Conditions and Heating Modes. *Earth Space Sci.* **2019**, *6*, 1749–1768. [CrossRef]
13. Miyagoshi, T.; Kageyama, A.; Sato, T. Formation of sheet plumes, current coils, and helical magnetic fields in a spherical magnetohydrodynamic dynamo. *Phys. Plasmas* **2011**, *18*, 072901. [CrossRef]
14. Yin, L.; Yang, C.; Ma, S.Z.; Huang, J.Z.; Cai, Y. Parallel numerical simulation of the thermal convection in the Earth's outer core on the cubed-sphere. *Geophys. J. Int.* **2017**, *209*, 1934–1954. [CrossRef]
15. Šimkanin, J.; Kyselica, J.; Guba, P. Inertial effects on thermochemically driven convection and hydromagnetic dynamos in a spherical shell. *Geophys. J. Int.* **2018**, *212*, 2194–2205. [CrossRef]
16. Wicht, J.; Sanchez, S. Advances in geodynamo modelling. *Geophys. Astrophys. Fluid Dyn.* **2019**, *113*, 2–50. [CrossRef]
17. Long, R.S.; Mound, J.E.; Davies, C.J.; Tobias, S.M. Scaling behaviour in spherical shell rotating convection with fixed-flux thermal boundary conditions. *J. Fluid Mech.* **2020**, *889*, A7. [CrossRef]
18. Silva, L.; Gupta, P.; MacTaggart, D.; Simitev, R.D. Effects of shell thickness on cross-helicity generation in convection-driven spherical dynamos. *Fluids* **2020**, *5*, 245. [CrossRef]
19. Simitev, R.D.; Busse, F.H. Onset of inertial magnetoconvection in rotating fluid spheres. *Fluids* **2021**, *6*, 41. [CrossRef]
20. Shebalin, J.V. Mantle electrical conductivity and the magnetic field at the core–mantle boundary. *Fluids* **2021**, *6*, 403. [CrossRef]
21. Arnold, W.A.; Wilcox, W.R.; Carlson, F.; Chait, A.; Regel, L.L. Transport modes during crystal growth in a centrifuge. *J. Cryst. Growth* **1992**, *119*, 24–40. [CrossRef]
22. Ozoe, H.; Fujii, K.; Shibata, T.; Kuriyama, H.; Churchill, S.W. Three-dimensional numerical analysis of natural convection in a spherical annulus. *Numer. Heat Transf.* **1985**, *8*, 383–406. [CrossRef]
23. Hirano, H. *Nagare no Suuchikeisan to Kashika [Numerical Analysis and Visualization for Fluid Flow]*, 3rd ed.; Maruzen: Tokyo, Japan, 2011. (In Japanese)
24. Ueno, K. *Vector Analysis*; Kyoritsu Shuppan: Tokyo, Japan, 2010. (In Japanese)
25. Mersenne Twister with Improved Initialization. Available online: http://www.math.sci.hiroshima-u.ac.jp/m-mat/MT/MT2002/mt19937ar.html (accessed on 29 July 2022).
26. Ozoe, H.; Toh, K. A technique to circumvent a singularity at a radial center with application for a three-dimensional cylindrical system. *Numer. Heat Transf.* **1998**, *33*, 355–365. [CrossRef]
27. Ozoe, H. *Magnetic Convection*; Imperical College Press: London, UK, 2005.
28. Tagawa, T. Linear stability analysis of liquid metal flow in an insulating rectangular duct under external uniform magnetic field. *Fluids* **2019**, *4*, 177. [CrossRef]
29. Tagawa, T. Effect of the direction of uniform horizontal magnetic field on the linear stability of natural convection in a long vertical rectangular enclosure. *Symmetry* **2020**, *12*, 1689. [CrossRef]
30. Masuda, T.; Tagawa, T. Linear stability analysis of three-dimensional natural convection at low Prandtl number in an annular enclosure in the presence of a toroidal magnetic field. *AIP Adv.* **2020**, *10*, 125208. [CrossRef]